ABSTRACT

Title of Document:	NUMERICAL SIMULATION OF A MICROFABRICATED GAS PRECONCENTRATOR FOR ENVIRONMENTAL MONITORING
	Jonathan Christopher Day, Master of Science, 2005
Directed By:	Professor Christopher Cadou, Aerospace Engineering

A numerical simulation of the separation of gaseous species through a microfluidic gas preconcentrator has been performed. The gas preconcentrator is a curved converging/diverging nozzle that operates like a gas centrifuge. The preconcentrator is being developed to enhance the sensitivity of microscale gas sampling devices for fast response, on-site environmental monitoring. The numerical model solves the Euler equations and the Maxwell-Stefan diffusion equation to provide an exit mass flux profile for a particular set of inlet conditions. From this profile, the efficiency of the preconcentrator is determined by computing the separation factor, which measures the ability of the device to separate the gas flow into two streams that are depleted and enriched in the heavy gas molecule. The results of the simulations are compared to experimental measurements of the separator's performance and provide insight into the underlying physics of the operation of the preconcentrator.

NUMERICAL SIMULATION OF A MICROFABRICATED GAS PRECONCENTRATOR FOR ENVIRONMENTAL MONITORING

By

Jonathan Christopher Day

Thesis submitted to the Faculty of the Graduate School of the
University of Maryland, College Park, in partial fulfillment
of the requirements for the degree of
Master of Science in
Aerospace Engineering
2005

Advisory Committee:
Professor Christopher Cadou, Chair
Professor James Baeder
Professor Benjamin Shapiro

© Copyright by
Jonathan Christopher Day
2005

Dedication

I would like to dedicate this thesis to my loving family. To my wife, I could never have completed this work without your never ending support and patience. To my daughter, I want to thank you for always having a smile on your face. It always lightens up the room and my life.

Acknowledgements

I would like to thank my committee chair and advisor Dr. Christopher Cadou, my committee members Drs. James Baeder and Benjamin Shapiro, Dr. Ghodssi and Sheng Li for their work on the design and experimental testing of the device, and my professors and fellow students at the University of Maryland.

Table of Contents

List of Tables

List of Figures

Chapter 1: Introduction

1.0 Overview

This thesis describes the use of computational fluid dynamics (CFD) to understand the operation of a fast-response microfluidic gas concentrator being developed for environmental monitoring applications. The concentrator uses the same operating principles as a gas centrifuge and is capable of providing short time-scale (<0.01 millisecond), continuous, gas concentration and separation.

1.1 Motivation

The ability to detect airborne contaminants/pathogens is critical to ensure the safety of military and civilian personnel. Current technology requires that air samples be collected on site and then transported to a remote laboratory for testing. This limits the frequency and overall quality of the sampling process [1]. These limitations stem from the fact that the equipment required to collect and analyze the samples is bulky and expensive. What is required is a compact air sampling and analysis system that is fast, simple, rugged, and inexpensive enough to be used on site and be integrated with some kind of warning system. The successful development of miniaturized chemical processing plants for DNA sequencing that have compressed a laboratory's worth of analysis equipment onto a single silicon wafer suggest that similar approaches could be used to develop a miniaturized chemical/biological sensor.

1.2 Enabling Technologies

Two key technologies are responsible for the development of chem/bio labs-on-a-chip: Micro Electro Mechanical Systems (MEMS) fabrication processes and Microfluidics.

1.2.1 MEMS Fabrication

Microelectromechanical systems (MEMS) are systems of electronic and non-electronic microscale elements that perform functions that can include signal acquisition (sensing), signal processing, actuation, display, and control. They can also serve as vehicles for performing chemical and biochemical reactions and assays [2]. MEMS devices have been developed based on the microchip fabrication process of photolithography with enhancements through specialized micromachining techniques. Lithography provides the ability to manipulate in-plane geometries to the sub-micron level. The use of etching, thin-film deposition, and wafer-bonding allow for the expansion of these two-dimensional geometries into three-dimensional devices.

1.2.2 Microfluidics

A microfluidic device is a MEMS device that is focused on the manipulation and/or sensing of a working fluid [3]. A key feature of microfluidic devices is the ability to gain a mechanical advantage and/or evaluate a sample with the usage of a minimal amount of fluid (typically in the range of a nano- to pico-liter) [4]. Due to this minimum fluid requirement and the reduced size of the related equipment (e.g.

valves and pumps), microfluidic devices provide the potential for a higher level of integration with mechanical and electrical devices than previously attainable. Other advantages provided by the reduction in size are a lower device weight, higher portability, lower power requirements, and faster assay times.

The development of microfluidic devices has focused on the development of complete biological and/or chemical laboratories on a single microchip or "lab-on-a-chip" devices. The work was pioneered by Manz et al. and Harrison et al. [5], [6] and has seen significant growth and advancements in the past few years. The inherent potential of microfluidic devices has been shown in the development of the "lab-on-a-chip" micro total analysis system by Srinivasen et al. [7] to run chemical microreactors for capillary electrophoresis assays (Simpson et al. 1998) [8] and red blood cell rigidity tests (Brody et al. 1995) [9].

1.3 Limitations of Current Technology

One important aspect of determining air quality is detecting volatile and semi-volatile chemical vapors within the gas sample. Several portable direct-reading instruments (e.g. miniaturized mass spectrometers) currently exist [10-12] for this purpose. However, they lack the sensitivity to accomplish routine air quality monitoring. For example, the miniaturized mass spectrometer determines gas composition by ionizing the gas, passing it through a magnetic field which turns the gas molecules by various radii of curvature determined by their charge to mass ratios, and by measuring the ion abundances at the location where they impact the detector. The main causes of the low sensitivity level in this device are variations in the electric

field that cause changes in the radii of curvature and the miniaturization of the device which lowers the mass resolution by lowering the area available for dispersion on the detector.

1.4 Part of the Solution: Preconcentration

1.4.1 Conceptual Overview

A possible solution to the low sensitivity of existing miniaturized detection systems is the addition of a preconcentrator. A preconcentrator is a device that converts a sample containing a low mole percent of a species of interest into a sample with smaller volume but having a higher mole percent of the species of interest. Increasing the concentration of the sample makes detection of the species easier. Several macroscopic sensitivity enhancement techniques have had microscopic versions developed. These include chromatography [10, 13, 14], sorbent beds [15-17], and selectively-permeable polymer diaphragms [18, 19]. However, each of these methods is relatively slow (approximately 10 minutes for separation) due to the time constants associated with adsorption/desorption of the gas on the elements or the diffusion of the species through the chromatography media. In addition, some of these methods require temperature controls and utilize consumable materials for the concentration process. These requirements increase the complexity of the devices and make them more difficult to integrate into compact sensing systems with the overall result being a larger, less portable, and less reliable device. These requirements also increase the complexity of device manufacturing which in turn increases its cost.

1.4.1.1 Gas Chromatography

In gas chromatography, the sample is mixed with a carrier gas and forced through a separation column which is typically a coiled stainless steel capillary filled with a high surface area inorganic or polymer packing (eg. polysiloxane). The mixture exiting the column is stratified into discrete bands of uniform chemical composition in order of increasing retention time in the column. Detection of the passage of the bands as they exit the column is usually accomplished by measuring the gas's thermal conductivity but other detections methods like flame ionization are also possible. The process is illustrated schematically in figure 1.1.

Micromachining techniques have been used to create miniature gas chromatographs [1,14] capable of separating vapor mixtures of up to 70 species with a response time of approximately 10 minutes and an accuracy level on the order of parts per billion (ppb).

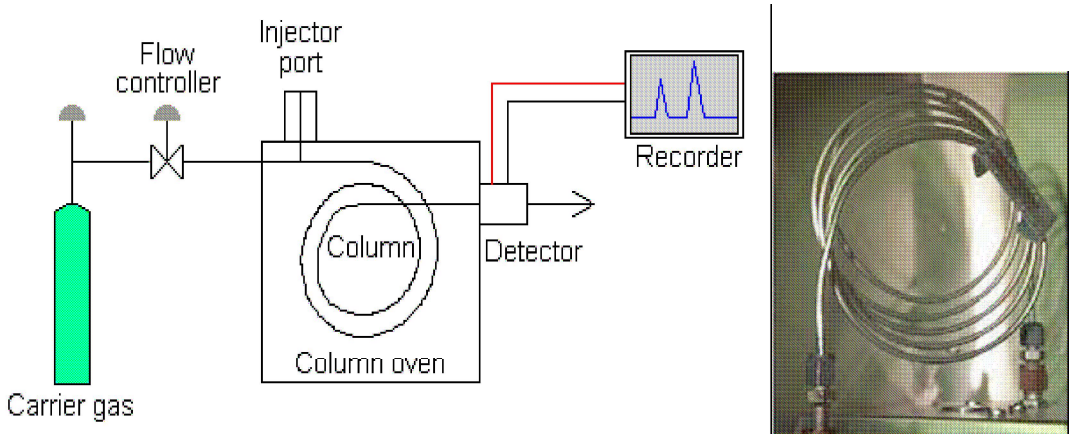

Figure 1.1: Schematic of a Gas Chromatograph with a photograph of the separation column [13]

1.4.1.2 Sorbent Beds

Sorbent bed preconcentrators are typically long glass capillary tubes filled with one or more adsorbent materials that adsorb in one direction and desorb in the other direction [15]. Conventional-scale devices require the glass tube to be heated, usually by a resistive heating element to 200 °C, for desorption. Tian et al [16, 17] have developed single and multiple stage preconcentrators for use with the miniature gas chromatographs described above. Their device is illustrated in figure 1.2 [15]. The preconcentrator consists of a thick micromachined silicon heater packed with a small quantity of a granular adsorbent material (i.e. roughly spherical granules of a high-surface-area, graphitized carbon). This device has shown separation resolution on the order of 0.2 ppb within approximately 8 minutes.

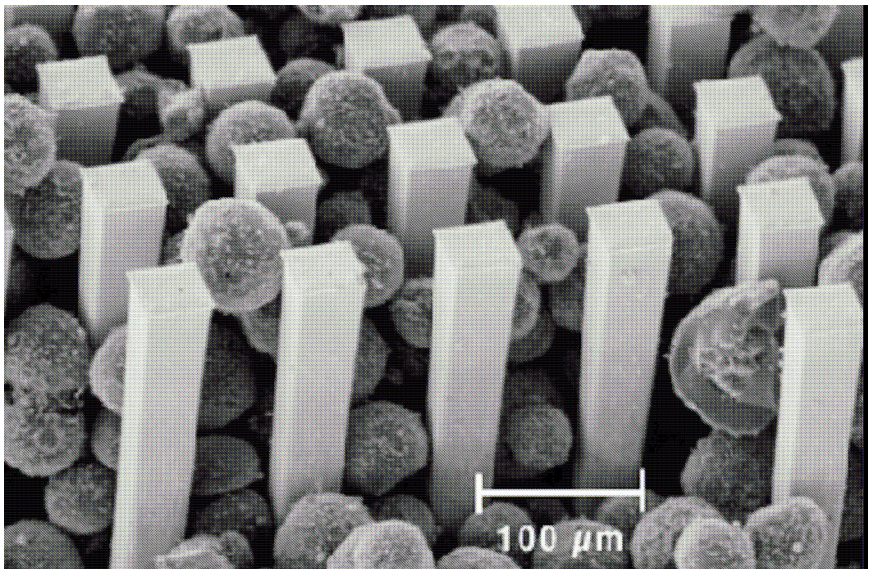

Figure 1.2: Scanning Electron Micrograph (SEM) of a Preconcentrator - consisting of a thick micromachined Si heater and graphitized carbon beads as adsorbents [15]

1.4.1.3 Selectively Permeable Membranes

Selectively permeable membranes, illustrated in figure 1.3, can be utilized as a preconcentrator by virtue of their ability to separate gas species by the differences in their solubility and diffusion rates though the membrane. The ability of the devices to concentrate the gas sample depends on the properties of the polymeric films. Effective materials exist and have been used for the construction of selectively permeable membranes [18, 19]. However, several drawbacks exist including the response times due to the "reservoir" effect of the polymer film and the necessity to use a specific polymer film to separate out a specific gas.

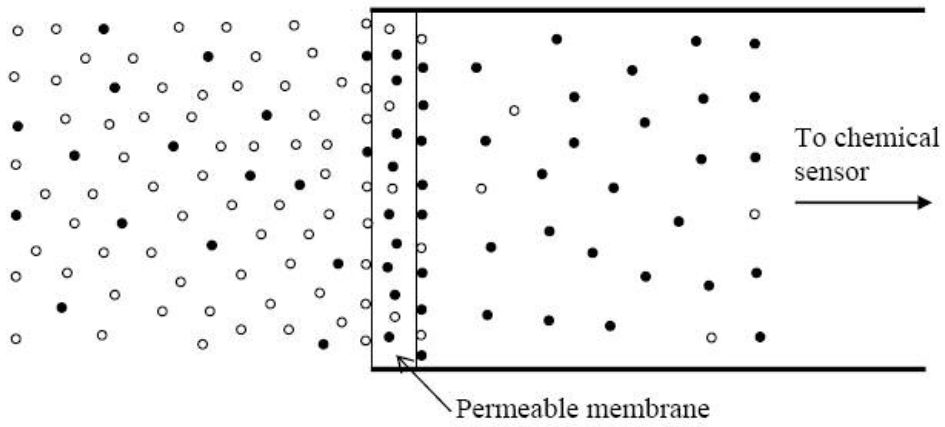

Figure 1.3: A Selectively Permeable Membrane - allowing selected gases to travel through it faster than others.

1.4.1.4 Converging/Diverging Nozzles

The use of a converging/diverging nozzle, see figure 1.4 [20], for the separation of $U^{235}F_6$ gas from $U^{238}F_6$ gas was originally proposed by Dirac [21]. Species separation within this device is based solely on the pressure gradients generated within the device with pressure driven diffusion forcing the denser species

into the higher total pressure region near the nozzle centerline and then separating the flow using a cylindrical skimmer.

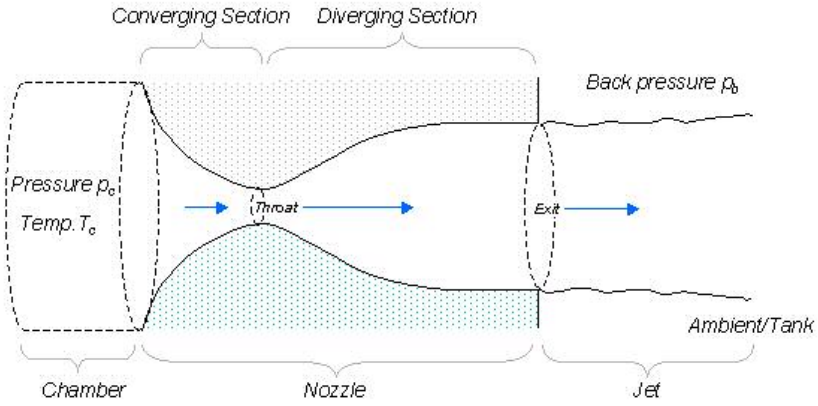

Figure 1.4: A Converging/Diverging Nozzle [20]

However, the initial attempts failed because they were missing two key design features proposed and implemented by Becker et al in the early sixties: a low molecular weight auxiliary gas [22] and a deflection wall [23] as illustrated in figure 1.5.

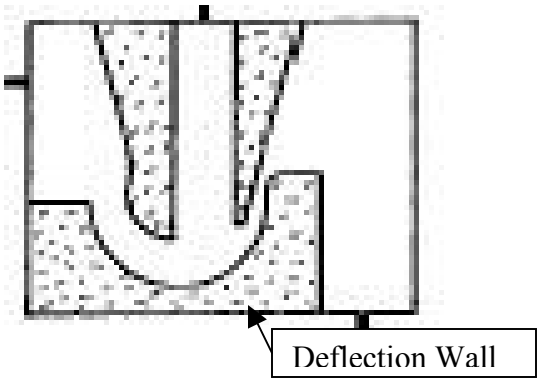

Figure 1.5: A Single-stage Gas Concentrating Element with Deflection Wall [24].

The use of a light auxiliary gas allows acceleration of the gas mixture to higher speeds because of the lower mean molecular weight of the mixture while the deflection wall creates a centrifugal field proportional to the square of this velocity. The higher speeds and the bending of the flow create a larger pressure gradient across the device which in turn creates a higher diffusive flux and therefore a larger separation factor. With the implementation of these changes, the separation nozzle has become a standard method for the separation and enrichment of U-235 [21, 24-26]. The current design mixes an auxiliary gas (e.g. nitrogen) with natural UF_6 and forces it through an array of separation nozzles by applying a pressure difference across the device. The flow accelerates as it is forced through the nozzle and this reduces the pressure within the device to approximately 1 millitorr. Arrays of these separation nozzles are capable of providing the necessary 3% enrichment for the creation of nuclear fuel [21].

1.4.2 Description of Device

The separation nozzle under investigation here is somewhat different from those used in Uranium separation. First, it is designed for use in an open system where the gas mixture flows continuously and is driven by a positive pressure upstream. Second, the molecule to be separated is Sulfur Hexafluoride (SF_6) as opposed to Uranium Hexafluoride (UF_6). Figure 1.5 is a 3-D contour image generated using an optical profilometer (Veeco WYKO NT1100) of the microfabricated device with the color scale (ranging from blue at 5 microns and red of 0 microns) depicting depth within the device.

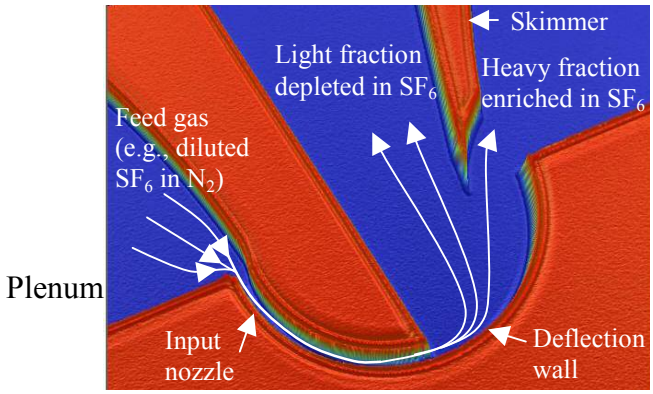

Figure 1.6: An Optical Profilometry Image of the Separation Device

It is a single stage device consisting of a plenum, a curved converging-diverging nozzle, a deflection wall, and a skimmer. A dilute mixture of SF_6 (1 mole %) in N_2 is introduced into the converging-diverging nozzle at a pressure of between 1 and 3 atmosphere and allowed to accelerate to supersonic velocities while being deflected radially. This deflection is continued by the curved deflection wall. The centripetal acceleration of the fluid associated with this continuous deflection creates a radial pressure gradient in the fluid stream which, in turn, forces the denser components to the outer part of the flow and the less dense components to the inner part of the flow. The skimmer divides the stratified flow into two streams that subsequently exit the device. The inner stream is called the light fraction because it is depleted in SF_6. The outer stream is called the heavy fraction because it is enriched in SF_6 [27].

1.5 Benefits of Miniaturization

The miniaturization of the gas separation nozzle provides several benefits compared to the alternative separation techniques previously mentioned and the

macroscopic version used in Uranium processing. The miniaturized separation nozzle has a short response time on the order of 0.01 milliseconds and does not require consumable materials or control of environmental conditions (e.g. temperature). It also requires a greatly reduced sample size and works with pressurized gas instead of a vacuum.

The need to operate at low pressure (i.e. a vacuum) in the macroscopic design comes from the fact that the flow must be in or near the slip regime for the device to work effectively. The slip regime corresponds to a flow situation where there is a finite tangential component of the gas velocity at the wall. The normal measure used to determine whether the flow is in the slip regime is the Knudsen number (Kn), which is the ratio of the mean free path of the gas particles (λ) to a characteristic dimension of the flow path (d).

$$Kn = \frac{\lambda}{d} \tag{1}$$

In this work, d is chosen to be the depth of the nozzle flow channel. The mean free path is estimated using the following equation [28]:

$$\lambda = \frac{1.26\mu\sqrt{RT}}{P} \tag{2}$$

In this equation, μ is the coefficient of dynamic viscosity for the gas mixture, R is the gas constant, T is the gas temperature, and P is the gas pressure. If this ratio is between 0.01 and 0.1, the flow is within the slip regime [29]. For the macroscopic device, whose length scale is approximately 100 millimeters, the only method

available to achieve the desired Knudsen number is to lower the gas pressure – typically to 50 millitorr. When the device is miniaturized with a flow passage depth of approximately 5 microns, however, the flow enters the slip regime at a much higher pressure (approximately several atmospheres). This pressure range is much more convenient because it allows the gas to be driven through the device under pressure and expanded to atmospheric conditions at the exit.

1.6 Objectives and Approach

The overall objective of this thesis is to use computational fluid dynamics (CFD) to understand the operation of a particular gas concentrator being developed for environmental monitoring applications and to verify experimental measurements of its performance. The specific objectives of the thesis are to:

- Identify the appropriate governing equations for the problem.
- Use a commercial CFD code to
    - Create a computational grid to represent the test article.
    - Solve the governing equations on the computational grid.
- Compare the predictions of the numerical simulation to the experimental measurements.

- Explain the results by identifying the underlying physical processes that govern the operation of the device.

- Make suggestions for how the performance of the device could be improved.

Chapter 2: Separation Nozzle Design, Fabrication, and Testing

2.1 Design

The basic design of the separation device is shown in figure 2.1. The gas is injected and removed from the system through capillary tubes attached to 500 micron diameter wells etched into the silicon substrate. The expanded view of the nozzle area shows the key design dimensions.

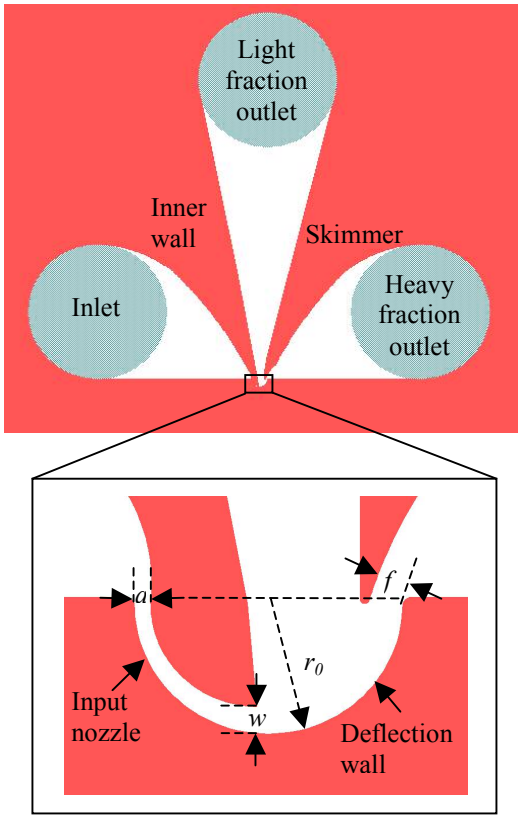

Figure 2.1: The Basic Separation Nozzle Design with Key Design Dimensions

These dimensions are the nozzle throat width (a), the nozzle exit width (w), the deflection wall radius (r_o), and the skimmer distance (f). In addition, the nozzle depth (d) is another key design dimension. Figure 2.2 shows a completed device with the Tygon tubing attached.

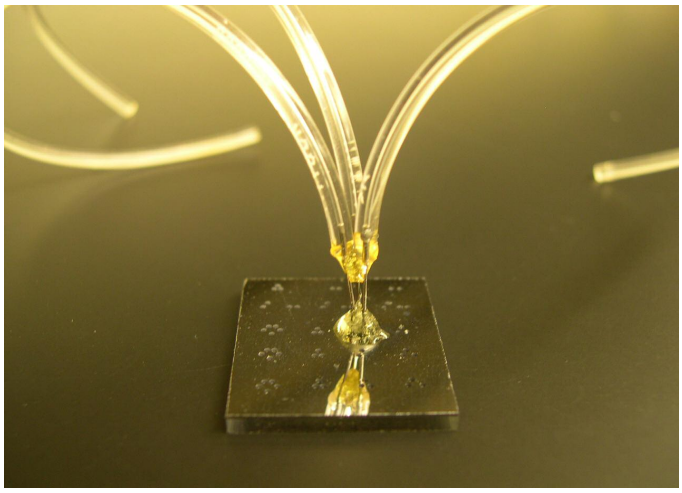

Figure 2.2: Picture of a Packaged Nozzle with Tygon Flexible Tubing

The values of the nozzle dimensions were selected based on the desired inlet pressure and mass flow rate. With a desired inlet pressure range of 1 to 3 atmospheres, the nozzle depth is set to 5 microns to keep the Knudsen number between 0.005 and 0.05. The nozzle throat width (a) was chosen to provide a mass flow rate of approximately 1 standard cubic centimeter per minute (sccm). This value was chosen to match the input flow rates of some of the existing miniaturized mass spectrometers [10, 11]. The relationship between the mass flow rate and the nozzle throat width is given by the expression for 1-D isentropic flow in a nozzle [28]:

$$a = \frac{\dot{m}}{d\sqrt{\gamma P \rho}}\left(\frac{2}{\gamma+1}\right)^{\frac{\gamma+1}{2(\gamma-1)}} \tag{3}$$

In this expression, ρ is the gas density, $\dot{m}$ is the mass flow rate, and γ is the ratio of specific heats. Based on (3), nozzle widths of 3.6 and 18.0 microns were experimentally tested. The exit nozzle width was set based on providing an expansion ratio of 1.69 allowing for an ideal exit Mach number as high as 2. The skimmer location was set at 20 microns from the deflection wall to maximize the separation factor of the nozzle. Only the 18.0 micron nozzle was simulated computationally because this configuration had the best performance.

2.2 Fabrication

In the past, the fabrication of isotope separation devices has relied on the tedious and costly methods of either stacking of photo-etched metal foils or the LIGA process [24-26]. The recent development of deep reactive ion etching (DRIE) and wafer-level bonding have provided alternative fabrication processes that are less costly and less tedious. The fabrication process for this device has six steps as shown in Figure 2.3. The first step is to grow a two micron thick silicon oxide film layer on the backside of a silicon wafer (step a). Next, a patterned 1.5 micron layer of photoresist (S1813, Shipley, Marlborough, MA) is developed to allow for the reactive ion etching (RIE) of the topside of the silicon wafer to create the 5 micron deep gas flow channels (step b). A 6 micron patterned layer of photoresist (AZ 9245, Clariant, Somerville,

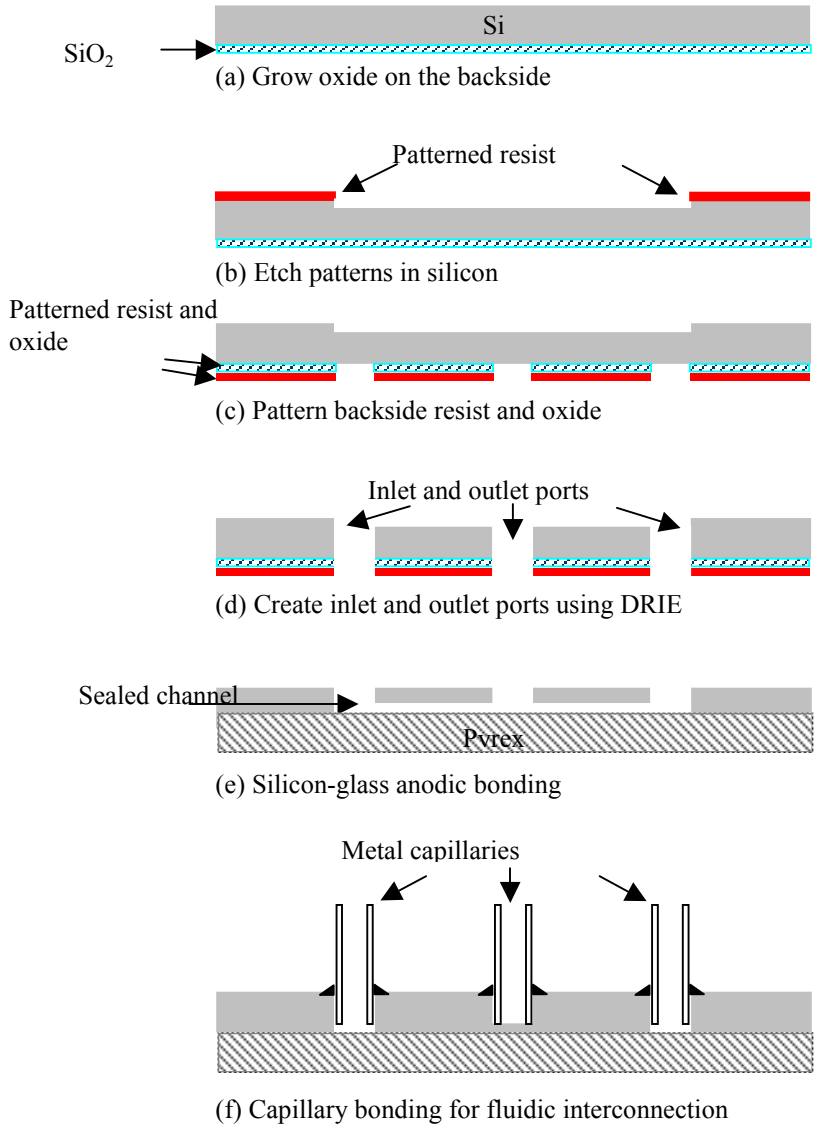

Figure 2.3: Device Fabrication Process including Fluidic Interconnections

NJ) is then applied to the back side of the wafer to define the locations of the inlet and outlet ports. Using the photoresist as a mask, the silicon oxide layer is etched with buffered HF (step c). The photoresist and the silicon oxide layers are then used as a mask for creating the inlet and outlet ports with DRIE (step d). After stripping the

photoresist and silicon oxide layers, anodic bonding is used to attach a Pyrex glass wafer to the backside of the silicon wafer to seal the flow channels (step e). The final step is to attach metal capillary tubes to the inlet and outlet ports to allow for gas insertion and extraction from the device (step f). The details of the method of attaching the capillary tubes are described in detail elsewhere [30]. The final chip after silicon-glass anodic bonding is shown in Figure 2.4. Note that the capillary tubes have not yet been attached in this figure.

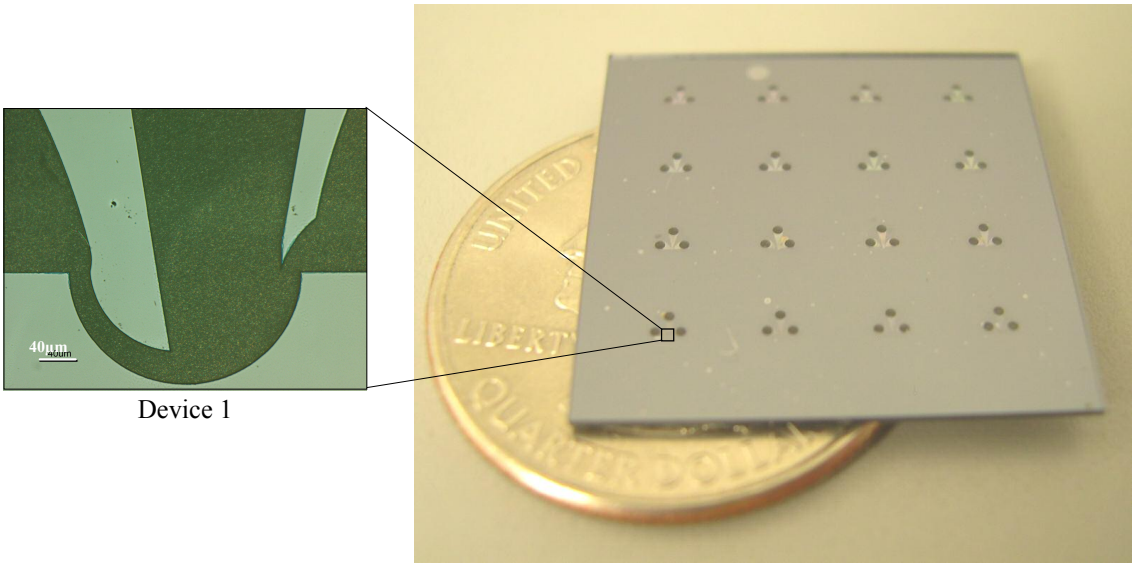

Figure 2.4: Final Device Configuration with a Close-up of the Curved Nozzle

2.3 Quantifying Separation Performance

The separation performance is quantified using the separation factor (A) which ranges from one (corresponding to no separation) to infinity (corresponding to perfect separation of the heavy element). The separation factor can also go to zero when

there is perfect "reverse" separation (i.e. the entire light species fraction ends up in the heavy stream). The separation factor is defined as follows for a binary mixture:

$$A = \frac{\theta_l(1-\theta_h)}{\theta_h(1-\theta_l)} \tag{4}$$

where θ_l and θ_h are the 'partial cuts' of the light and heavy species respectively. The partial cut of a component of the mixture is defined as the percentage of its throughput in the separation element, which is withdrawn in the light fraction stream. These can be written in terms of the mass flow rates of the heavy and light species in the heavy and light streams.

$$\theta_l = \frac{\dot{m}_{l,light}}{\dot{m}_{l,light} + \dot{m}_{l,heavy}} \quad \text{and} \quad \theta_h = \frac{\dot{m}_{h,light}}{\dot{m}_{h,light} + \dot{m}_{h,heavy}} \tag{5}$$

In this set of equations, θ_l is the partial cut of the light element (i.e. Nitrogen), θ_h is the partial cut of the heavy element (i.e. Sulfur Hexafluoride), and $\dot{m}$ is the mass flow rate. The first subscript in these equations, *l* or *h*, corresponds to the light species or the heavy species, respectively. The second subscript, '*light'* or '*heavy'*, corresponds to the light or heavy fraction stream respectively where the light fraction stream is the outlet nearest the center of the device and the heavy fraction stream is the outlet at the outer wall. For these definitions of the partial cuts, perfect separation of an element corresponds to $\theta_h = 0$. The success of the design of a separation device is directly related to its ability to maximize the separation factor.

2.4 Experiments

Gas separation experiments were conducted to examine the effect of operating conditions and geometric parameters on the separation factor of the fabricated devices. The experimental variables were the comparison of the gas mixture, the inlet pressure, and the nozzle geometry (i.e. the values of a, w, r_o, f, and d).

Table 2.1: Geometric parameters for two prototype gas concentrating devices

Device	Deflection Wall Radius	Nozzle throat width	Skimmer distance (μm)
1	120 μm	18.0 μm	20.0 μm
2	120 μm	3.6 μm	20.0 μm

Two gas mixtures were used throughout the experiments: 0.01 SF_6/0.99 N_2 molar mix and a 0.01 SF_6/0.99 Ar molar mix. The purpose of utilizing two gas mixtures was to investigate the effect of changing the molecular weight of the carrier gas. SF_6 was chosen as the heavy molecule because it is non-hazardous and its molecular weight of 146 amu is close to those of various organic contaminants including trichloroethylene (131.4 amu) and naphthalene (128.17 amu). N_2 was chosen as the auxiliary gas to simulate the properties of air. Separation performance was measured for inlet pressures ranging from 1 to 3 atmospheres. This range was selected because it is well within the capabilities of existing small air pumps. Two nozzle geometries were used throughout the experiment as given by table 2.1. However, only device 1 was computationally modeled as indicted earlier.

2.4.1 Apparatus

A schematic diagram of the experimental apparatus is shown in figure 2.5.

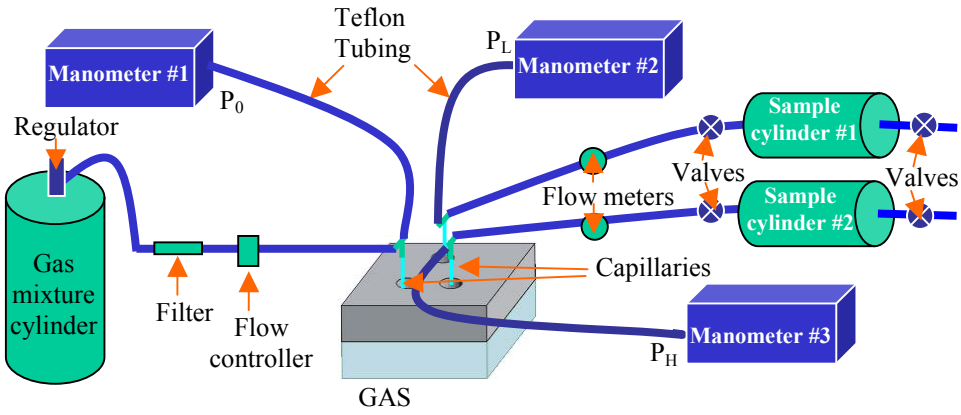

Figure 2.5: A schematic diagram of the experimental apparatus

The mixture to be separated is stored in a pressurized gas cylinder. The gas mixture was delivered to the device via a system of Teflon tubing. The mass flow of the mixture was regulated by a HFC-302 (Teledyne Hastings Instruments, Hampton VA) mass flow controller. A 0.5 micron filter removes particles that could clog the separator. The inlet pressure was regulated using the pressure regulator on the gas bottle and measured using an MKS model 722A manometer (MKS Instruments, Andover, MA). The pressures at the heavy and light fraction outlets are measured using MKS model 622A manometers. The mass flow rates in the outlets are measured using HFM-300 mass flow meters (Teledyne Hastings Instruments, Hampton VA). Samples from the heavy and light fraction outlets are collected in two 10 cm^3 stainless steel cylinders (SS-4CD-TW-10, Nupro Corporation, Solon, OH).

The composition of the samples is determined using mass spectrometry [31]. Figure 2.6 shows the gas analysis setup which consists of a mass spectrometer (Transpector CIS TS200, Inficon, East Syracuse, NY), a vacuum chamber, a turbomolecular pump, and a mechanical pump (not shown in the figure).

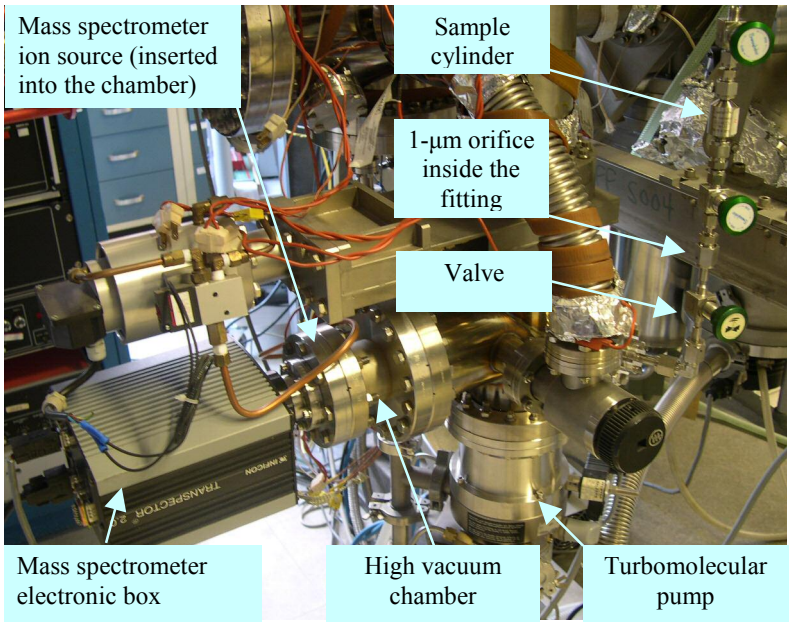

Figure 2.6: The Mass Spectrometer Gas Analysis Setup

The sample cylinder is connected to the vacuum chamber through a 1 micron orifice. This limits the flow so that adequate vacuum may be maintained to achieve effective electron ionization. The mass spectra of the samples are then evaluated to determine the composition of the gas. Comparing the composition of the gas in the heavy and light fraction samples to the composition of the original mixture enables the determination of the separation factor.

2.4.2 Experimental Procedure

The gas separation experiments were conducted by attaching pressurized gas canisters containing the desired gas mixture to the experimental setup shown in figure 2.5. The flow controller is then adjusted to begin flowing the gas mixture through the

separation nozzle. After the necessary purge time to force the air out of the system (typically 30 minutes), the valves are closed to collect samples from the heavy and light fraction streams. Throughout this period, the upstream and downstream pressures are monitored to maintain the desired pressure ratio. The gas sample cylinders are then taken to be analyzed using the mass spectrometer setup shown in figure 2.6. A more detailed description of the experimental setup and procedure along with a description of the error estimate methodology are provided in [32].

2.5 Typical Experimental Results

The final result from each experiment is a relationship between the pressure ratio across the device and the separation factor as defined by equation 4. A typical set of results is shown in Figure 2.7.

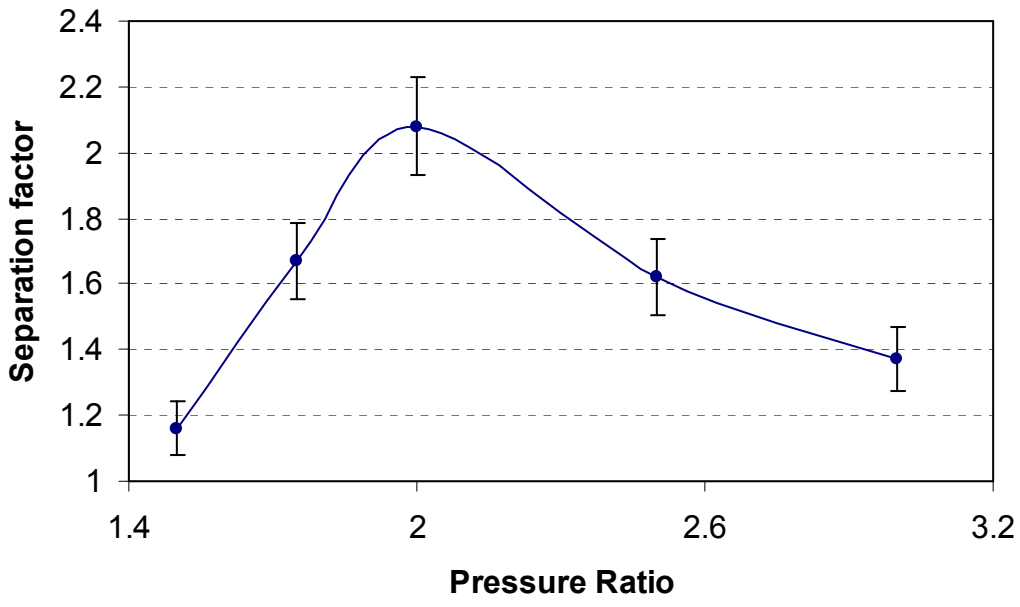

Figure 2.7: Typical Experimental Results Showing Separation Factor vs Pressure Ratio

Chapter 3: Computational Model

The flow field in the device is governed by the inlet-to-outlet pressure ratio and the geometry of the converging-diverging nozzle. Of particular interest are the effects of the small dimensions (i.e. velocity slip at the walls) on the development of the boundary layer. The development of this boundary layer is important because the radial pressure gradient is proportional to the square of the gas velocity and it is the radial pressure gradient that drives the pressure diffusion process responsible for stratifying the flow.

3.1 Governing Equations

There are six independent variables associated with the flow through the separation device: the x- and y-component velocities, the gas density, the gas pressure, the gas temperature, the mass fraction of SF_6, and the mass fraction of N_2. Therefore, determining the flow field requires solving six governing equations. Since carrying temperature as an additional variable simplifies the statement of the governing equations, the total number of equations to be solved increases to seven.

The flow of fluid in the device is described by the 2-D time-invariant, compressible Euler equations [33] plus the equation of state for an ideal gas [34].

$$\left(\vec{u}\cdot\vec{\nabla}\right)\rho+\rho\vec{\nabla}\cdot\vec{u}=0 \tag{6}$$

$$\left(\vec{u}\cdot\vec{\nabla}\right)\vec{u}+1/\rho\vec{\nabla}\rho=1/\rho\,\vec{F} \tag{7}$$

$$\left(\vec{u}\cdot\vec{\nabla}\right)p+\gamma p\vec{\nabla}\cdot\vec{u}=\left(\gamma-1\right)\left(Q-\vec{u}\cdot\vec{F}\right) \tag{8}$$

$$p=\rho RT \tag{9}$$

In these expressions, $\vec{u}$ is the velocity vector, γ is the ratio of specific heats (C_p/C_v) for the gas mixture, Q is a net heat generation per unit volume (equal to zero here) and $\vec{F}$ is a body force vector (also equal to zero here). Equation 6 represents conservation of mass, equation 7 represents conservation of momentum (and counts for two equations because it has x and y components) and equation 8 represents conservation of energy.

As indicated earlier, the diffusion of heavier particles to the outer wall and lighter particles to the inner wall of the device is driven by the radial pressure gradient associated with the turning of the gas flow. However, there is also a reverse diffusion process opposing separation which is driven by the concentration gradient. This condition is typical of a centrifuge. However, the key difference between the process occurring in a centrifuge and the process occurring in this device is that the centrifuge is a closed system whereas the separation nozzle is an open system. As a result, the sample is only under the influence of the pressure gradient for a very short time. The balance between pressure, concentration, and thermal diffusion is given by the generalized Maxwell-Stefan diffusion equation [34] for a two-component mixture.

$$J_A^*=-cD_{AB}\left[x_A\nabla\ln a_A+\frac{1}{cRT}\left[\left(\phi_A-\omega_A\right)\nabla p-\rho\omega_A\omega_B\left(g_A-g_B\right)\right]+k_T\nabla\ln T\right] \tag{10}$$

In this expression, $J_\alpha{}^*$ is the diffusive flux of species α, c is the concentration, $D_{\alpha\beta}$ is the binary mixture diffusion coefficient, x_α is the mole fraction of α, a_α is the activity of component α, g_α is the body force applied to species α, φ_α is the volume fraction of α, and ω_α is the mass fraction of α. The activity of the species is a corrected concentration value that provides the proper value of the free energy value and is defined by the following equation [35]:

$$d\overline{G}_\alpha = RTd\ln a_\alpha \tag{11}$$

In most cases, the activity is equal to the concentration. In this equation, $\overline{G}_\alpha$ is the partial molar Gibbs free energy, R is the universal gas constant, T is the temperature, d is the differential operator, and a_α is the activity of component α.

The diffusion equation is simplified for these calculations by converting the flux into a time derivative and by making the assumptions that it is a binary mixture and that the pressure and concentration diffusion terms are significantly larger than the external force and thermal diffusion terms. Applying these assumptions, the final diffusion equation is given by:

$$\rho\frac{\partial w_\alpha}{\partial t}+\nabla\cdot\left(-\rho w_\alpha D_{\alpha\beta}\left(\nabla x_\beta+\left(x_\beta-w_\beta\right)\frac{\nabla p}{p}\right)\right)=-\rho\vec{u}\cdot\nabla w_\alpha \tag{12}$$

The seventh and final governing equation comes from the requirement that all of the material within the device be either SF_6 or N_2. Therefore,

$$w_\beta = 1-w_\alpha \tag{13}$$

These equations (6-9, 12, 13) fully define the problem of determining the flow field within the computational domain set by the nozzle geometry.

3.2 Boundary Conditions

The computational domain used for the model is shown in figure 3.1 which shows the locations of the inlet, the light and heavy fraction outlets, and all of the other walls including the deflection wall and the skimmer.

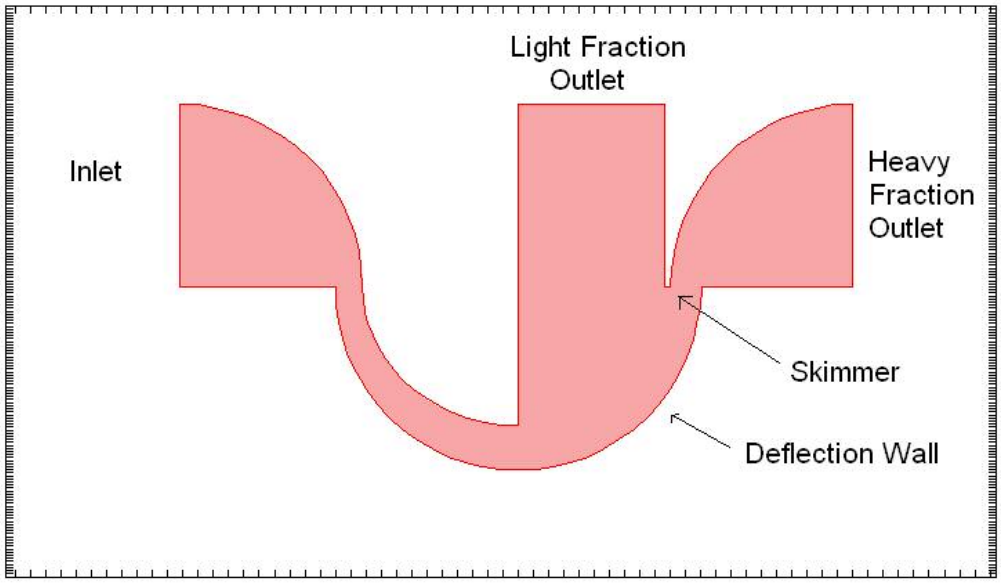

Figure 3.1: The Computational Domain used for Modeling

3.2.1 Wall Conditions

The boundary conditions for the device were set as no material flux through the wall (14) and a finite slip velocity at the wall (15) determined by the perfect slip assumption (i.e. there is no shear stress at the wall).

$$\hat{n} \cdot \vec{N} = 0; \vec{N} = -\rho w_1 \sum_{k=1}^{2} D_{1k} \left(\nabla x_k + \left(x_k - w_k \right) \nabla p / p \right) + D^T \nabla T / T + \rho w_1 \vec{u} \qquad (14)$$

$$\hat{n} \cdot \vec{u} = 0, \quad \vec{t} \cdot \left(-p\vec{I} + \eta \left(\vec{\nabla} \vec{u} + \left(\vec{\nabla} \vec{u} \right)^T \right) \right) = 0 \qquad (15)$$

In these expressions, $\hat{n}$ is a unit vector normal to the surface and pointing out of the enclosed volume, $\vec{t}$ is a unit vector that is tangent to the surface, and $\vec{I}$ is the identity vector.

3.2.2 Inlet/Outlet Conditions

Conditions at the inlet were set as follows: The mass fractions of SF_6 and N_2 were 5% and 95% respectively. The Mach number at the inlet was 0.2 in the x-direction and 0 in the y-direction. The non-dimensional fluid density was 1 and the non-dimensional inlet pressure varied from 1 to 3. The outlet boundary conditions required that the convective mass flux be normal to the exit area (16) and that the non-dimensional pressure equaled 1 along the exit plane.

$$\vec{n} \cdot \vec{N} = 0; \vec{N} = -\rho w_1 \sum_{k=1}^{2} D_{1k} \left(\nabla x_k + \left(x_k - w_k \right) \nabla p / p \right) + D^T \nabla T / T \qquad (16)$$

3.3 Solution Method

The governing equations are solved subject to the boundary conditions using a commercially available software package called FEMLAB ® that implements a finite element method. The software is especially convenient for this application because it allows the user to enter any governing equations in symbolic form and thereby control exactly which parts of the governing physics are included and excluded.

3.3.1 Specifying the Geometry

The software also includes a simple drawing environment which allows the user to describe the computational domain, generate the finite element mesh, and apply boundary conditions. Figure 3.2 shows the finite element mesh for a particular solution. FEMLAB ® uses adaptive gridding so the meshes for each set of flow conditions are different.

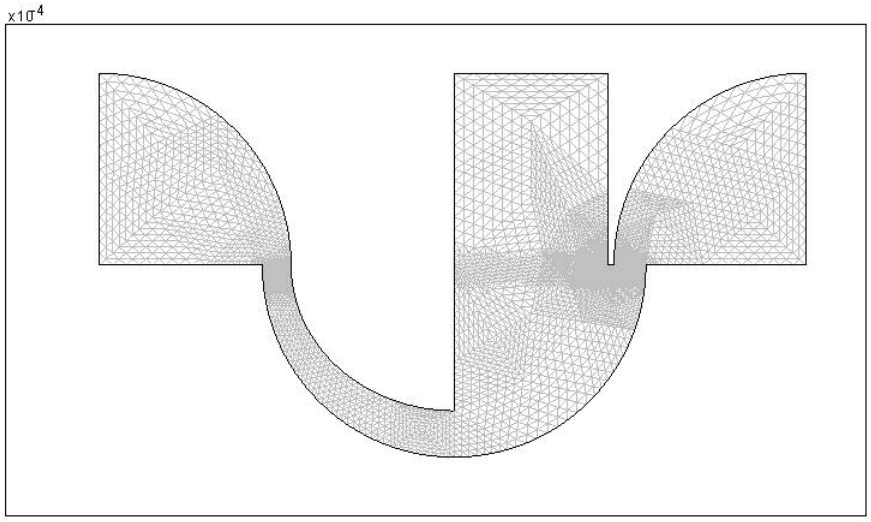

Figure 3.2: A Typical Finite Element Mesh for the Model Geometry with ¼ of the Mesh Points Displayed.

3.3.2 Specifying the Boundary Conditions

The software allows for the specification of several types of boundary conditions at each boundary whether external or internal to the model geometry. The available boundary conditions are dependent upon the equations being solved. For the Euler equations, the boundary conditions can be inflow/outflow, slip/symmetry, or no conditions. For the Maxwell-Stefan diffusion equation, the available boundary conditions are no flux, convective flux, and fixed mass fraction. In this study, only

the external boundaries conditions are imposed. The specific boundary conditions utilized were previously discussed in sections 3.2.1 and 3.2.2.

3.3.3 Solving the Governing Equations

The software offers a wide array of solvers including linear and non-linear, direct and iterative, steady-state and time-dependent, and parametric solvers. FEMLab also provides the ability to solve for the weak, general, or coefficient solution form. Since the problem under consideration is a highly non-linear steady-state problem, an iterative, steady state non-linear solver is used. The solver utilizes an incomplete LU preconditioner and GMRES linear solver during the solution process.

3.3.3.1 Non-Linear Solver

The non-linear solver uses an affine invariant form of the damped Newton method as described by Deuflhard [36]. This method solves a linearized form of the governing equations where f(U) is the residual vector, U is the solution vector, U_0 is the initial guess, δU is the Newton step, and f'(U_0) is the Jacobian matrix:

$$f'(U_0)\delta U = -f(U_0) \tag{17}$$

Equation (17) is solved using a linear solver (described in section 3.3.3.2) to determine the vector δU. This vector is then used to calculate the next iterative guess using the equation:

$$U_1 = U_0 + \lambda \delta U \tag{18}$$

where λ is the damping factor. The damping factor is limited in range from a minimum value of 1e-8 to a maximum value of 1. The solver then calculates the relative error, $\vec{E}$, based on the value of U_1 using the following equation:

$$f'(U_1)\vec{E} = -f(U_1) \tag{19}$$

If the calculated relative error is greater than the previous iteration, the damping factor is reduced and a new value for U_1 is calculated. This process is repeated until either the relative error is lower than the previous iteration or the damping factor is reduced below the minimum allowable value. If a successful iteration is accomplished, the solver then completes the next Newton iteration.

3.3.3.2 Linear Solver with Preconditioner

The linear solver used to solve equation (17) is a restarted generalized minimum residual (GMRES) method as described by references [37, 38]. This linear solver is used in conjunction with a preconditioner. Preconditioners are matrices that are used to help reduce the stiffness of the initial problem and thereby reduce the time to convergence of the linear solver. They are applied to both sides of the basic linear equation ($Ax = b$) in an attempt to simplify the A matrix. The resulting equation is:

$$M^{-1}Ax = M^{-1}b \tag{20}$$

FEMLab offers several types of preconditioners that can be applied when using the GMRES linear solver. The preconditioner chosen here is the incomplete LU preconditioner [39, 40]. The incomplete LU method provides the best ability to converge for highly complex multi-physics problems but has the drawback of having

higher memory and time requirements. The key feature of the LU method is that it creates the matrix, M, through the determination of a lower diagonal matrix (L) and upper diagonal matrix (U) that, when applied to the following equation (21) in which E is an error matrix, approximates the matrix A.

$$M = LU + E \approx A \tag{21}$$

The key parameter determining the success of the incomplete LU preconditioner is the drop parameter. The drop parameter sets which values in the preconditioning matrix are ignored (set to zero). The trade-off is between a faster convergence time (more dropped values) and the ability to converge to a solution at all (fewer dropped values). The drop parameter can be defined as a set lower limit on the value of any element in the matrix or it can be set so that a fixed percentage of the elements will be dropped based on their relative value to other elements in the same row of the matrix regardless of their magnitude. For this model, a fixed lower limit value drop parameter was utilized. This value was adjusted throughout the modeling process to achieve the fastest possible convergence while maintaining the models ability to converge. The drop parameter ranged from 0.01 to 1e-5.

3.3.3.3 Artificial Diffusion

Artificial diffusion is used to help maintain a stable solution throughout the iterative process by damping instabilities. The FEMLab software offers several methods for introducing artificial diffusion. These include isotropic diffusion, streamline diffusion, crosswind diffusion, and pressure stabilization. Neither crosswind nor pressure stabilization are used in this work.

Isotropic diffusion adds a coefficient of artificial diffusion to the diffusion already in the problem at the location of high gradients. The key advantage of isotropic diffusion is that it is most successful at limiting the impact and magnitude of local instabilities. However, its use also reduces the order of accuracy of the solution from second order to first order in the locations in which the artificial diffusion coefficient is used.

The streamline and crosswind diffusion methods add artificial diffusion along the flow streamlines and perpendicular to the streamlines, respectively. The method of introducing artificial streamline diffusion is the streamline upwind Petrov-Galerkin (SUPG) method. The key advantage of the SUPG method is that it does not perturb the initial equations. The addition of crosswind diffusion is accomplished by adding additional terms to the SUPG method.

One convenient aspect of FEMLab is that different types of artificial diffusion can be applied to different governing equations. The artificial diffusion methods utilized in this work are isotropic and streamline diffusion for the Euler equations. There is no artificial diffusion utilized for the solution of the diffusion equation.

3.3.3.4 Convergence Criteria

The convergence criteria for the solver are determined by the weighted Euclidian (L-2) Norm [41]:

$$err = \left(\frac{1}{N} \sum_i \left(\frac{E_i}{W_i} \right)^2 \right)^{1/2} \tag{22}$$

In this expression, N is the number of degrees of freedom, W_i are the weighting factors, and E_i are the error vector components.

3.3.3.5 Model Grid Mapping

The meshing used for the nozzle model was an unstructured grid of triangular elements. The initial meshing of the device was extremely coarse to allow for the solution to utilize an adaptive mesh. The benefits of the adaptive meshing method is an increased ability to converge to a solution because it leads to initial conditions at each mesh update that are more accurate and requires fewer grid points because they are judiciously located. The lower number of grid points also reduces the memory requirements for the model. The adaptive meshing algorithm [42] then regenerates the mesh by increasing the number of grid points at the locations of the highest error values.

Chapter 4: Results

Understanding of the ability of the separation nozzle to concentrate a heavy species in a gas mixture first requires understanding the flow field within the device. The specific flow field generated is governed by the device geometry and the applied boundary conditions, specifically the pressure ratio (defined as the inlet pressure divided by the outlet pressure) and the inlet SF_6 mass fraction. The device geometry creates several key flow features that occur regardless of the applied boundary conditions. Therefore, these features and their impact on the flow parameters will be discussed independent of the boundary conditions. Once these geometry dependent features are understood, it will be easier to understand the impact the boundary conditions have on the flow field. Throughout this discussion, several planar cuts will be discussed including cuts along the inlet, the nozzle throat, the diverging section exit, and the skimmer. The location and direction of these cuts are illustrated in figure 4.1.

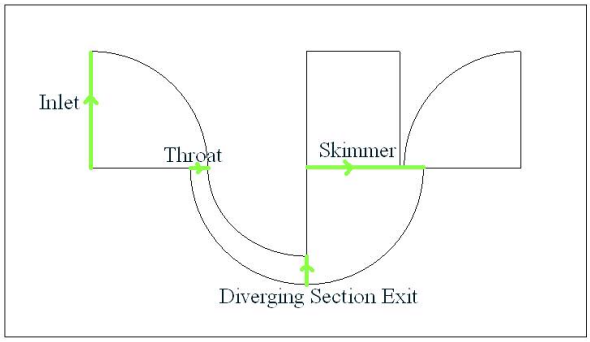

Figure 4.1: Planar Cuts Utilized within the Nozzle Geometry

The device geometry can be broken into three main sections: the converging/diverging section, the deflection wall section, and the skimmer section. A typical flow field generated by this geometry is shown in figure 4.2 with the key flow features labeled.

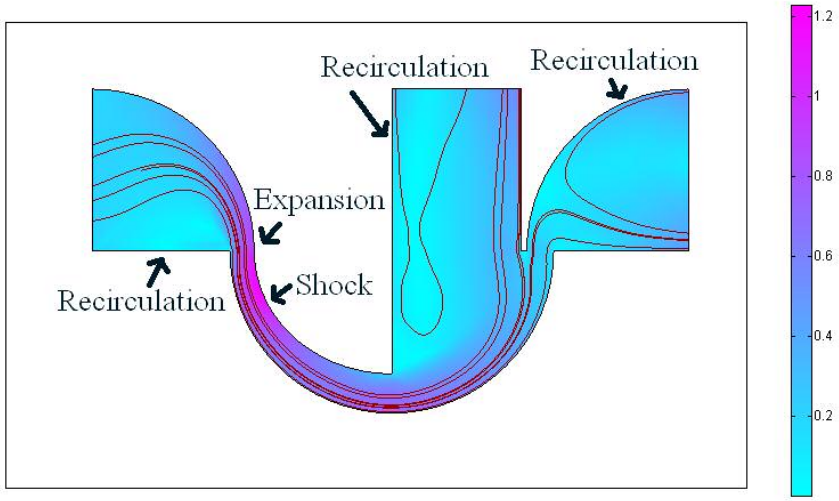

Figure 4.2: Flow Mode 1 Mach number Distribution with Superimposed Streamlines (Pressure Ratio of 1.75)

The converging portion of the nozzle is where the flow enters the device and is compressed and turned through 90 degrees. A key feature of the flow is the recirculation region along the straight wall. This recirculation region is generated because the straight wall acts like a forward-facing step in the flow field. The next flow feature within the converging/diverging section is the rapid expansion generated at the nozzle throat. The expansion is followed by a shock wave that stabilizes within the diverging section.

A recirculation region forms opposite the deflection wall behind the rearward-facing step at the nozzle exit.

The final section is the skimmer region. The skimmer section contains two geometric features that influence the flow: an airfoil (the skimmer) and the backward-facing step opposite the deflection wall (the heavy fraction outlet). The interaction of these two features generates a unique situation in which there appears to be two possible flow modes. The first mode has the flow hitting the skimmer straight on at nearly zero angle of attack as shown in figure 4.2.

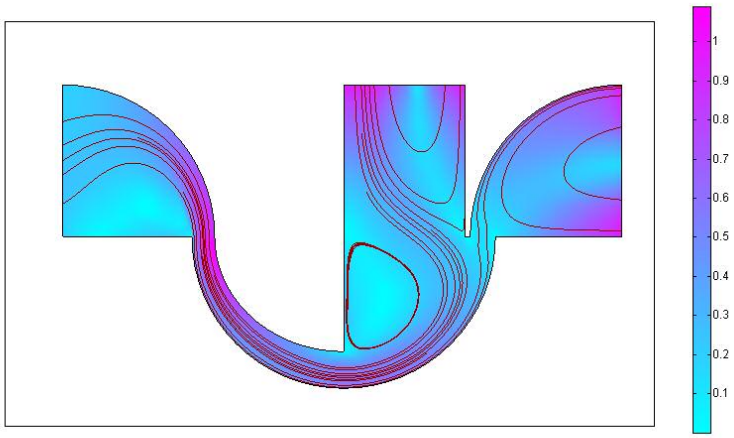

Figure 4.3: Flow Mode 2 Mach number Distribution with Superimposed Streamlines (Pressure Ratio of 1.75)

The second flow mode corresponds to a situation where the flows associated with the two geometric features do interact. This is illustrated in figure 4.3. The flow in this case is dominated by the redirection of the flow prior to hitting the skimmer at a non-zero angle. The change in the angle of attack between the flow direction and the

skimmer creates two significant changes in the flow pattern. The first feature is the splitting of the recirculation zone created within the expansion region into two separate counter-rotating vortices. The second feature is the lack of the redirection of the flow within the heavy fraction. Instead, the flow continues along the curved wall to the exit. This relocates the recirculation region within this area to the flat wall. The effects of these changes in the flow structure are higher flow velocities within both exit regions and a large increase in the separation factor due to the increased curvature of the streamlines.

The two flow modes were identified by using two different solution methods. The first mode is generated by using the weak solution mode for the governing PDEs. The second mode is generated by using the general solution mode for the governing PDEs. The difference between the two modes is that the weak solution guarantees the use of an exact Jacobian. The methodology behind the weak solution method and a comparison of these two solution modes is included in Appendix A.

An investigation was completed to determine if either or both of these flow modes were physically meaningful and, if so, which was more likely to be realized within the device. The test utilized to determine whether the flow modes were physically meaningful was to determine the entropy change within the device for each of these flow modes. The results of this test show that both flow modes meet the requirement that entropy increases throughout the device. The entropy changes are shown in figures 4.4 and 4.5 for modes 1 and 2, respectively.

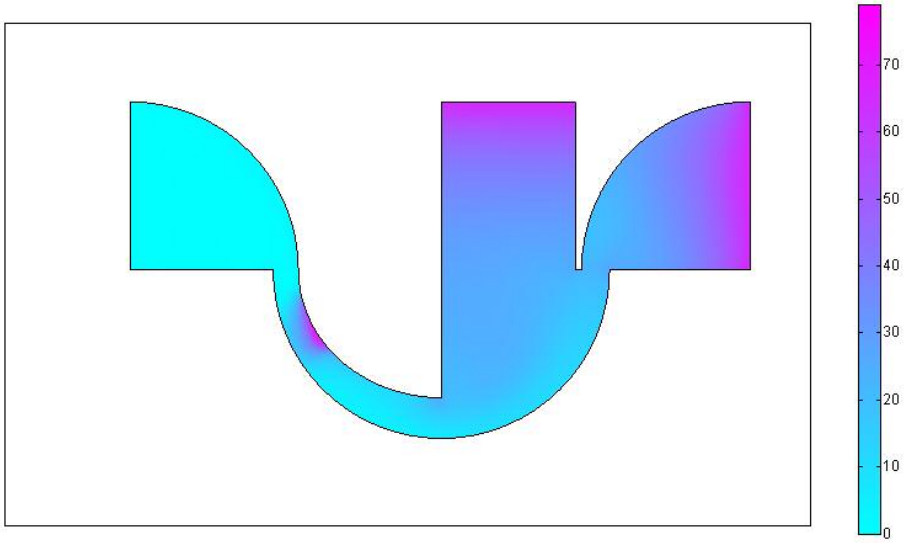

Figure 4.4: Mode 1 Entropy Change Contours for a Pressure Ratio of 1.75

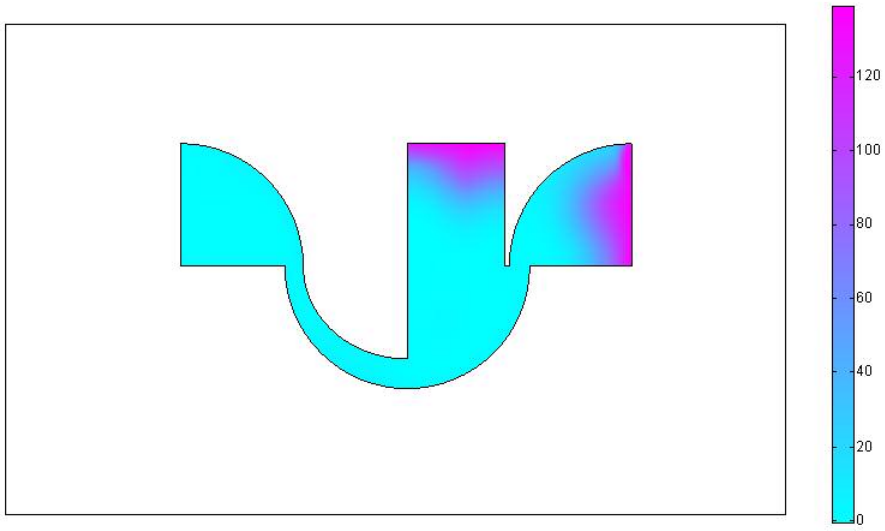

Figure 4.5: Mode 2 Entropy Change Contours for a Pressure Ratio of 1.75

Another test used to determine which flow mode was more likely to occur in the device was a comparison to the solution of the compressible Navier-Stokes equations without species transport at a pressure ratio of 1.75, illustrated in figure 4.6. This comparison was made because internal frictional forces are expected to be important in the actual flow. This test also provides a way to check the accuracy of the Euler equation's assumption of no viscous losses. The ability to utilize the Euler equations lowers the necessary computing power and stiffness of the computational model compared to solving the compressible Navier-Stokes equations along with the diffusion equations.

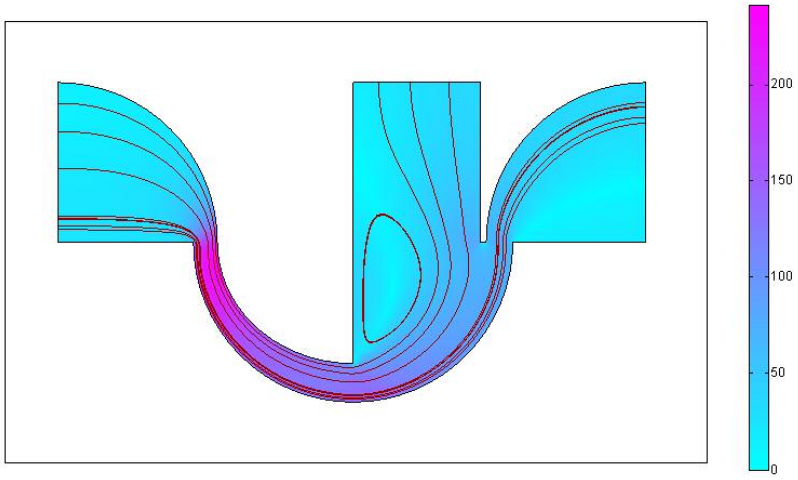

Figure 4.6: Navier-Stokes Mach number Distribution with Superimposed Streamlines (Pressure Ratio of 1.75)

Figures 4.2, 4.3, and 4.6 show that the flow structure in flow mode 1 is very similar to the results of the Navier-Stokes simulation. The differences between the results from the Navier-Stokes simulation and the first flow mode are that the expansion at the

nozzle throat is straight across the throat and the recirculation region within the light fraction stream ends prior to the outlet boundary. The differences between the Navier-Stokes simulation and flow mode 2 are more significant as they include the difference within the throat, the addition of a second recirculation region within the light fraction stream, and the existence of supersonic flow within both outlet streams. Therefore, it is more likely that the correct solution is that arrived at through the use of the weak solution mode which generates flow mode 1. In addition, the second flow mode includes high velocity values within the outlet streams which are not expected to occur within these regions. Therefore, for the rest of the simulations and model results, flow mode 1 will be utilized. However, the qualitative similarities between the Navier-Stokes simulation and the weak solution suggest that the assumption of no viscous losses is acceptable.

4.1 Pressure Distribution

The pressure distribution corresponding to the flow field shown in figure 4.2 along with a close up view of the nozzle throat area are shown in figure 4.7.

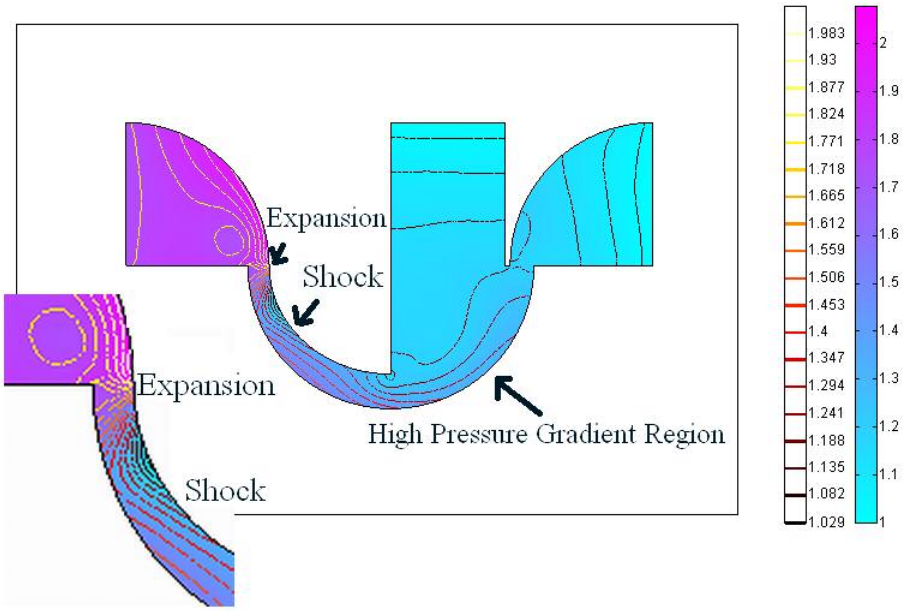

Figure 4.7: A Typical Mode 1 Static Pressure Distribution with Pressure Contours (Pressure Ratio of 1.75)

The key features within the pressure distribution are the expansion at the nozzle throat, the shock generated within the diverging section, and the area of high pressure gradients generated along the deflection wall. The location of the expansion is set by the nozzle geometry. The shape of the pressure gradient and the location where this area of large pressure gradient detaches from the deflection wall play a key role in the separation efficiency of the device.

4.2 Mach Number Distribution

The Mach number distribution, shown in figure 4.2, provides insight into the cause of the higher mass flow rate through the heavy fraction stream. As expected, the Mach number increases through the converging nozzle section and then reaches

supersonic values after the expansion through the nozzle throat. The Mach number is then reduced below 1 after the shock wave in the diverging portion of the nozzle. The nozzle geometry does create a unique general shape to the velocity profile due to the competing effects of the turning of the flow, which usually would lead to a higher velocity at the outer wall, and the higher molecular weight at the outer wall, which would lead to a lower velocity. As illustrated in figure 4.8 (see figure 4.1 for the planar cut locations), the velocity profile within the diverging section is governed by the higher molecular weight causing the high velocity region to be against the inner wall. However, at the end of the diverging section, the higher velocities are seen along the deflection wall.

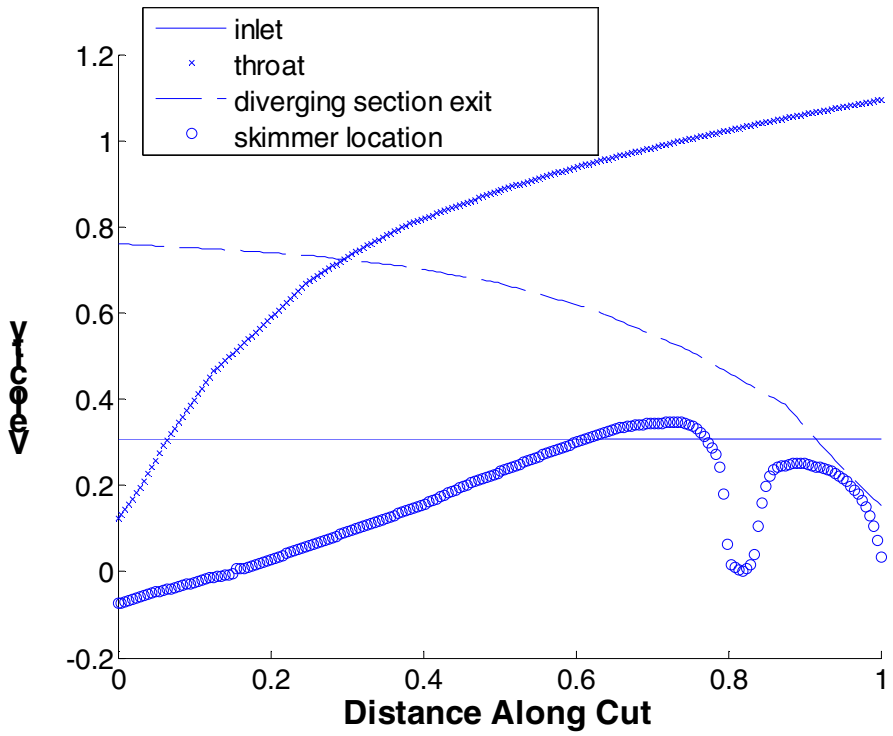

Figure 4.8: Velocity Profiles for Various Cuts within the Nozzle Geometry for a Pressure Ratio of 1.75.

4.3 Mass Fraction Distribution

The SF_6 and N_2 mass fraction distributions, shown in figures 4.9 and 4.10 respectively, illustrate the overall structure of the concentration field in the separation device.

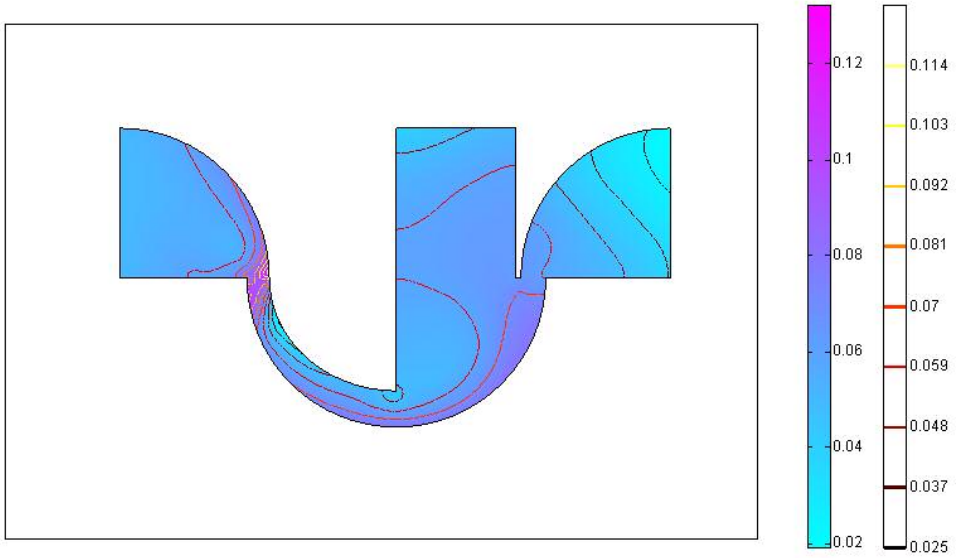

Figure 4.9: A Typical Mode 1 SF_6 Mass Fraction Distribution with SF_6 Mass Fraction Contours (Pressure Ratio of 1.75)

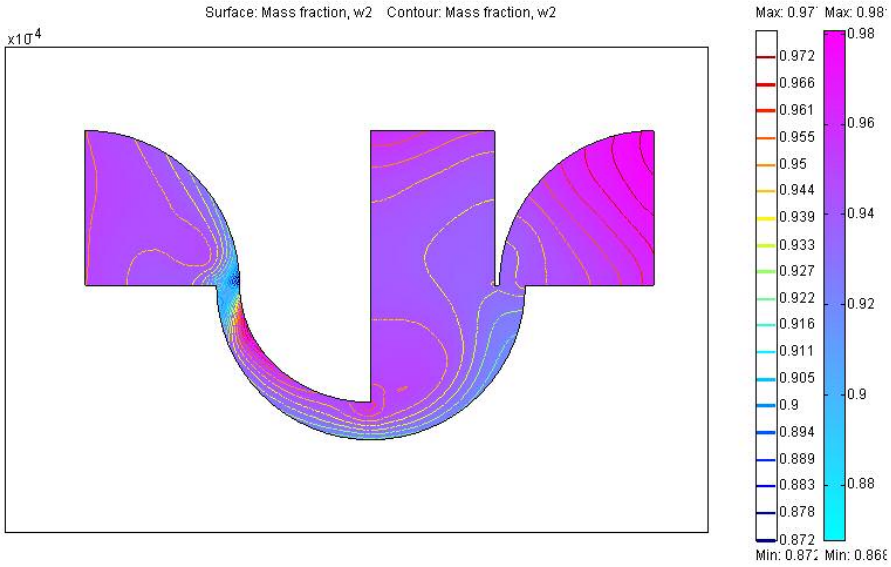

Figure 4.10: A Typical Mode 1 N_2 Mass Fraction Distribution with N_2 Mass Fraction Contours (Pressure Ratio of 1.75)

The denser species, SF_6, is driven to locations of highest pressure by centripetal acceleration and pressure diffusion. These locations correspond to the outer walls of each of the turning regions which means that the turn to enter the nozzle concentrates SF_6 on the inner wall and the subsequent turn in the oppositely curved nozzle and deflection wall causes the SF_6 to flow across the channel and become concentrated near the outer wall. This diffusive transport of SF_6 widens and distorts the expansion region. This distortion of the expansion through the throat is not seen in the Navier-Stokes simulation, as illustrated in figure 4.11, because the gas composition is not taken into account.

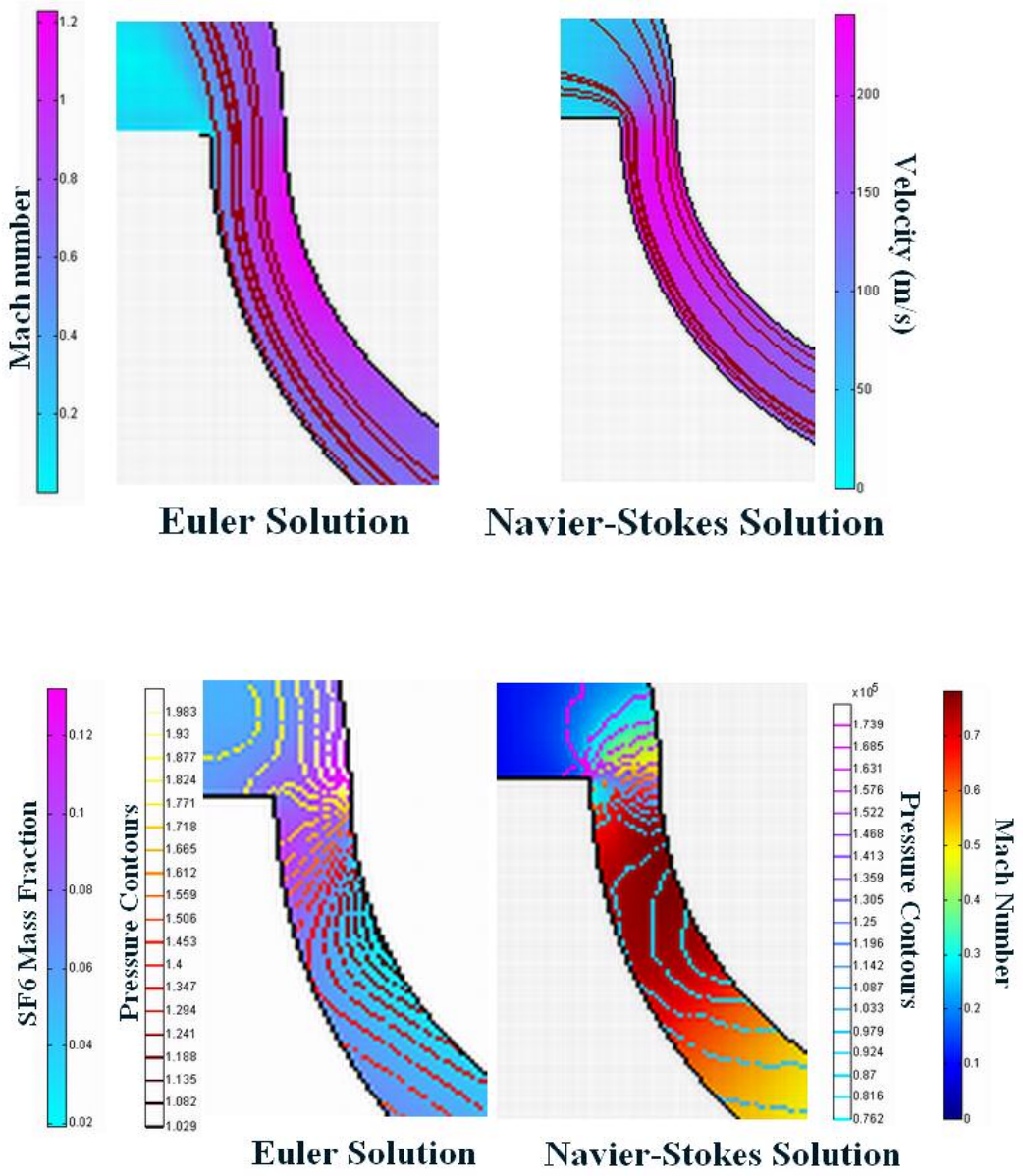

Figure 4.11: Comparison of the Shape of the Expansion and Shock Regions within the Diverging Section.

4.4 Mass Flux Distribution

The SF_6 and N_2 mass flux distributions, shown in figures 4.12 and 4.13, demonstrate the key features of the flow that lead to the separation.

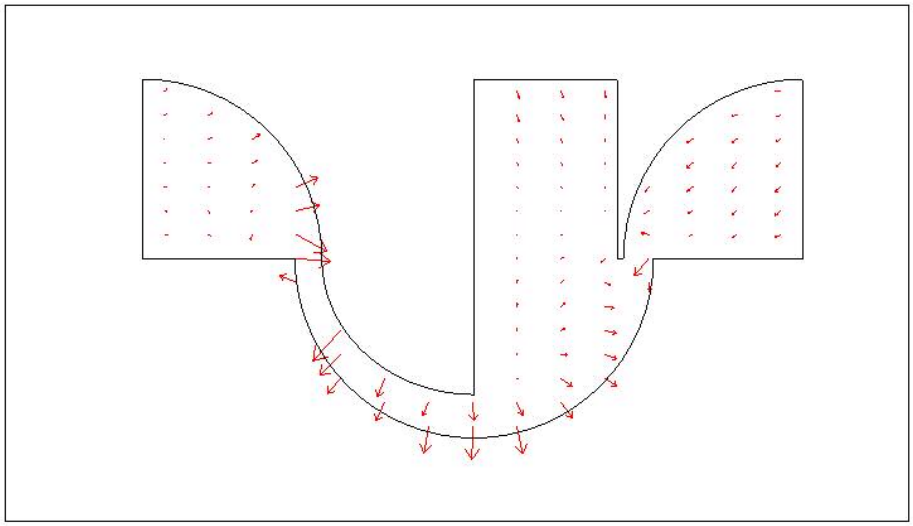

Figure 4.12: A Typical Mode 1 SF_6 Mass Diffusive Flux Vector (Pressure Ratio of 1.75)

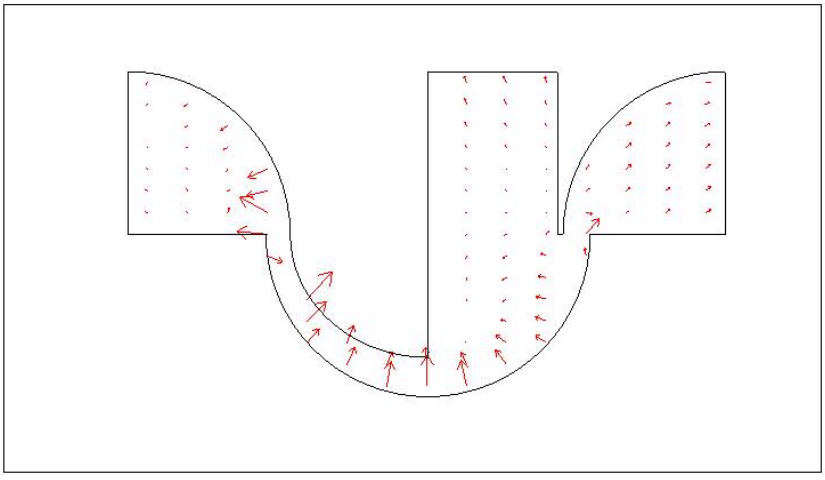

Figure 4.13: A Typical Mode 1 N_2 Mass Diffusive Flux Vector (Pressure Ratio of 1.75)

As shown in all three curved sections, the SF_6 flux moves steadily to the outer wall while the N_2 is pushed into the center of the flowstream. The other area of high diffusive flux occurs at the nozzle throat. The reversal of the direction of the pressure gradient at the nozzle throat forces the SF_6 to move back across the nozzle throat. This high flux region is the cause of the deformation of the expansion. This could also be manipulated to increase the overall separation efficiency of the device. The simulations indicate that when the flow is more stratified before it enters the throat, the SF_6 is able to diffuse back across the throat region more quickly and this, in turn, leads to improved separation.

4.5 Separation Factor

The separation factor is the key measure of the device's functionality and its definition was given previously in equation (4). The separation factor was calculated from the computational results by taking a cut at the skimmer location (shown in figure 4.1) and recording the mass fraction fluxes of N_2 and SF_6 along this cut at 2000 equally spaced locations. The data is shown in figure 4.14. This data was then used to calculate the total flow rates of SF_6 and N_2 through the light and heavy fraction streams by integrating across the respective flow areas.

$$\dot{m}_{l,i} = d\int_0^{R_L} \rho Y_i (\vec{u}\cdot\hat{n})dx \qquad \dot{m}_{h,i} = d\int_{R_L}^{R_H} \rho Y_i (\vec{u}\cdot\hat{n})dx \tag{25}$$

The integrations described by equation (25) were accomplished using a MATLab script that provides the net flux of the species *i* across the skimmer cut. This is equivalent to taking the cut at the actual device outlets because mass must be conserved.

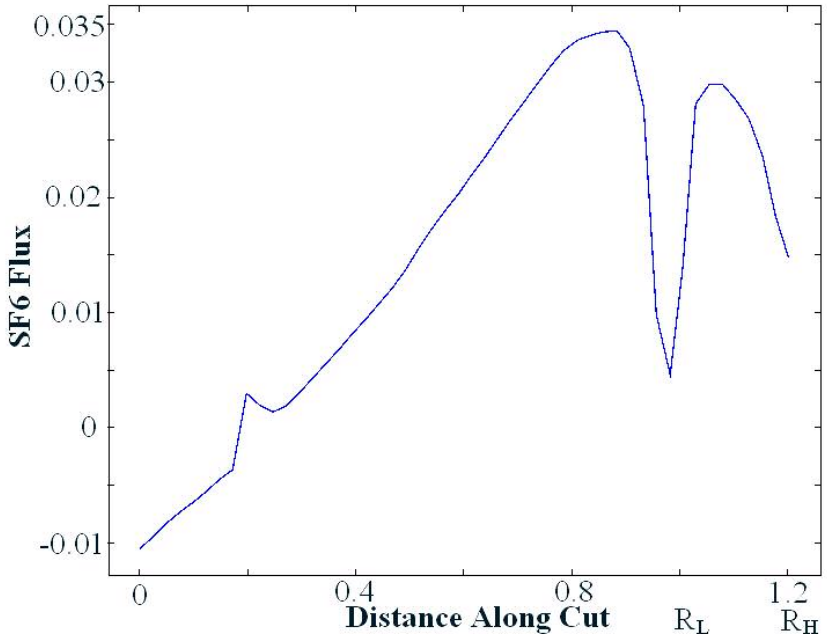

Figure 4.14: The SF_6 Mass Flux across the Skimmer Planar Cut for Mode 1 with a Pressure Ratio of 1.75

The results of the computational determinations of the separation factor for device 1 are presented in figure 4.15 as a plot of separation factor as a function of pressure ratio. The inlet mass fraction of SF_6 is 1 mole %. The two curves correspond to the two different flow modes observed. The curves peak at different pressure ratios and show that mode 2 seems to be associated with better separation performance than mode 1. The reasons for this are explained below.

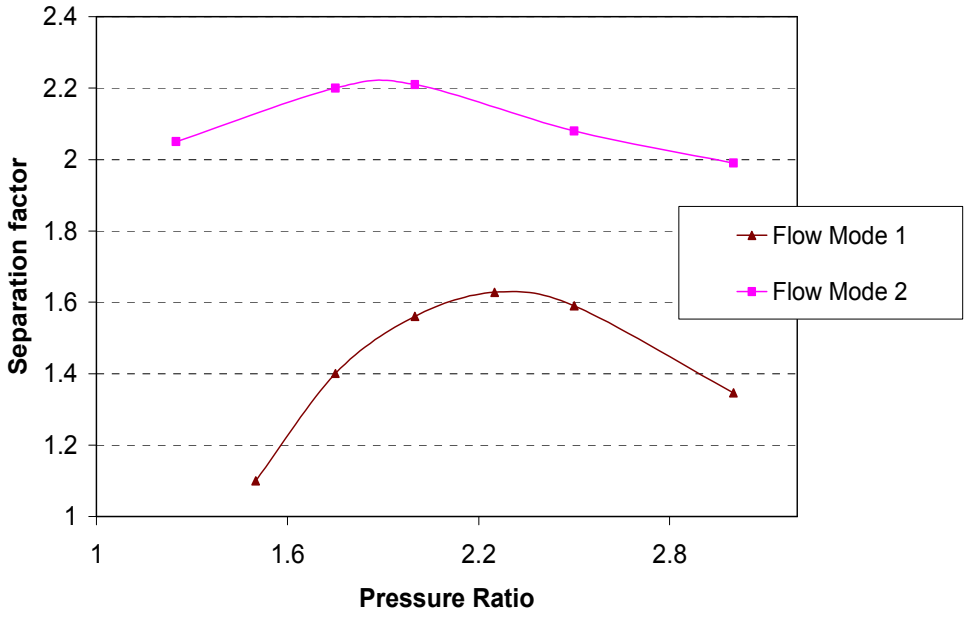

Figure 4.15: Plot of Separation Factor vs Pressure Ratio

4.6 Explanation of the Separation Process

4.6.1 Mach Number Distributions (Mode 1)

The Mach number distributions for pressure ratios of 1.75, 2, and 2.5 are shown in figures (4.2, 4.16, and 4.17) respectively. These profiles show that the expansion at the nozzle throat grows as the pressure ratio increases. At low pressure ratios, the location of the shock within the diverging section is close to the expansion at the nozzle throat. However, as the pressure ratio is increased, the shock moves downstream in the diverging section of the nozzle. The Mach number profile also more clearly shows the separation of the flow lines from the deflection wall at the higher pressure ratios. Another key flow parameter that is shown through the Mach number profiles is the size of the recirculation zone within the two exit regions.

Figures (4.2, 4.16, and 4.17) show that the recirculation zone within the light fraction grows and shifts further to the center of the exit region as the pressure ratio is increased.

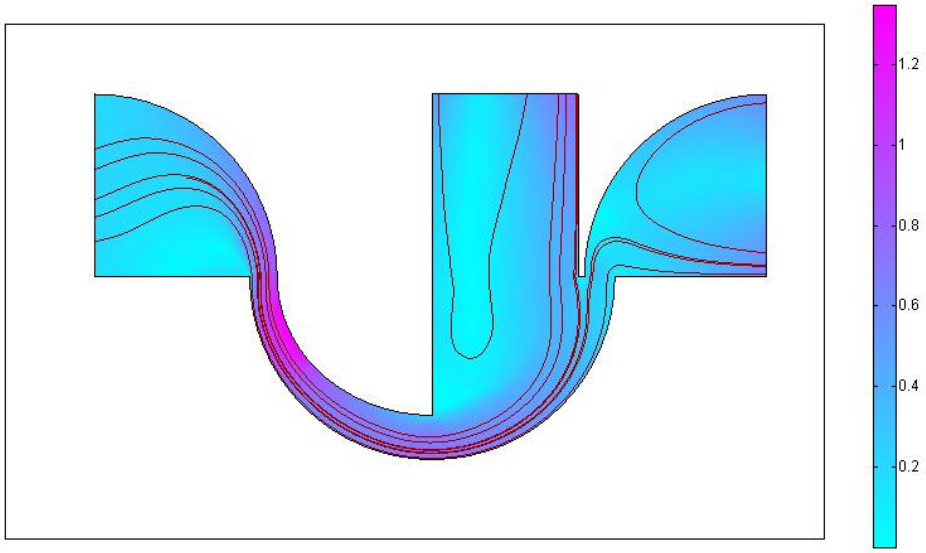

Figure 4.16: The Mode 1 Mach number Distribution for a Pressure Ratio of 2.0 with Streamlines

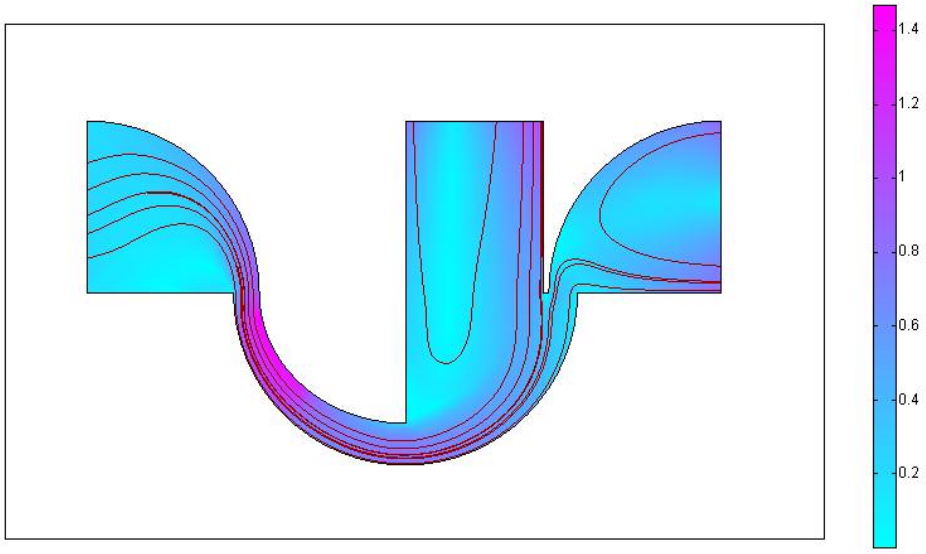

Figure 4.17: The Mode 1 Mach number Distribution with Streamlines for a Pressure Ratio of 2.5

4.6.2 Pressure Distributions (Mode 1)

The pressure distributions for pressure ratios of 1.75, 2, and 2.5 are shown in figures (4.7, 4.18, and 4.19) respectively. These figures show that the cause of the peak in the separation factor appears to result from a competition between two effects influenced by increasing the pressure ratio. The first effect is that the pressure gradients near the deflection wall spread further towards the center of the device as the pressure ratio is increased. As the gradients spread past the radius of the skimmer, the separation factor is decreased. The second effect is that the magnitude of the pressure gradients increases with increasing pressure ratio. The larger pressure

gradients generate a higher pressure-driven diffusive flux increasing the separation factor. At low pressure ratios (<1.75), the high pressure gradient area remains small and near the deflection wall throughout the expansion region. However, the pressure gradients are low and therefore generate a minimal amount of diffusive flux. At higher pressure ratios (>2.5), the region of high SF_6 concentrations becomes wider than the skimmer region and therefore the separation effects are not fully realized. At a pressure ratio of approximately 2, an optimum combination of high pressure gradient and the containment of the region of SF_6 enrichment within the skimmer radius provide the peak in the separation factor.

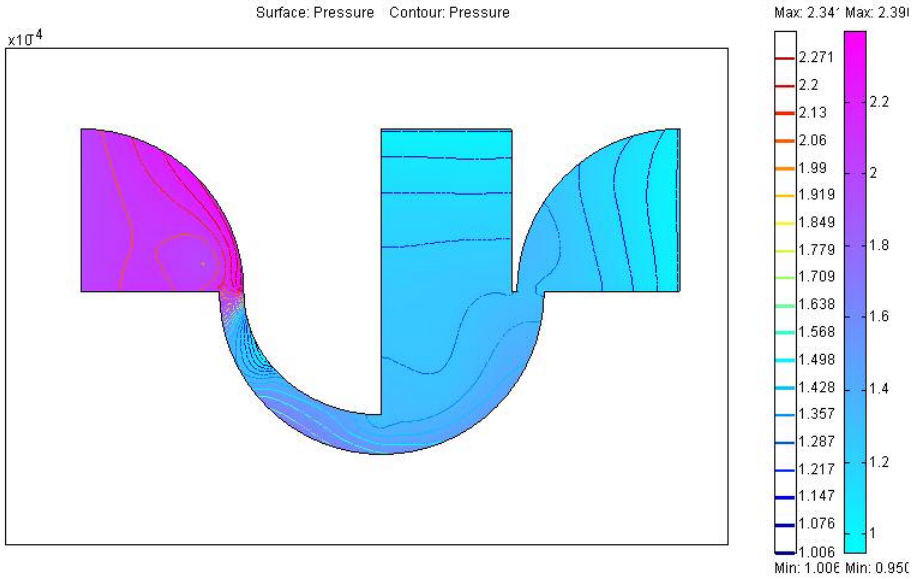

Figure 4.18: The Mode 1 Pressure Distribution with Pressure Contours for a Pressure Ratio of 2.0

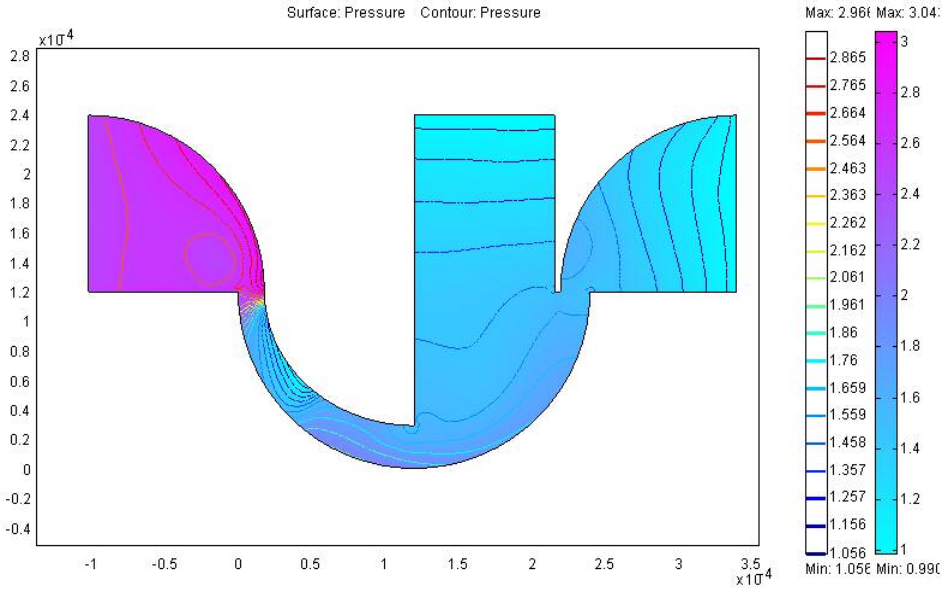

Figure 4.19: The Mode 1 Pressure Distribution with Pressure Contours for a Pressure Ratio of 2.5

4.6.3 Mass Fraction Distributions (Mode 1)

The SF_6 mass fraction profiles, shown in figures (4.9, 4.20, and 4.22), and the N_2 mass fraction profiles, shown in figures (4.10, 4.21, and 4.23), demonstrate how the mass fraction of SF_6 follows the pressure profile. At locations of higher pressures, whether created by the shock or the turning of the flow by the deflection wall, there is a higher concentration of SF_6 and therefore a lower concentration of N_2. As the pressure ratio is increased, the shape of the mass fraction profiles change in similar fashion to the changes in the pressure distribution discussed above.

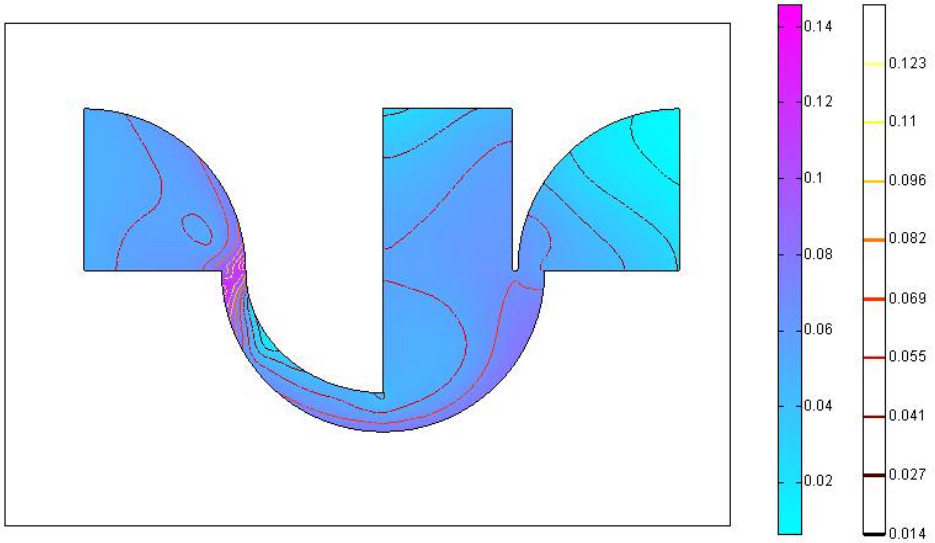

Figure 4.20: The Mode 1 SF_6 Mass Fraction Distribution with SF_6 Mass Fraction Contours for a Pressure Ratio of 2.0

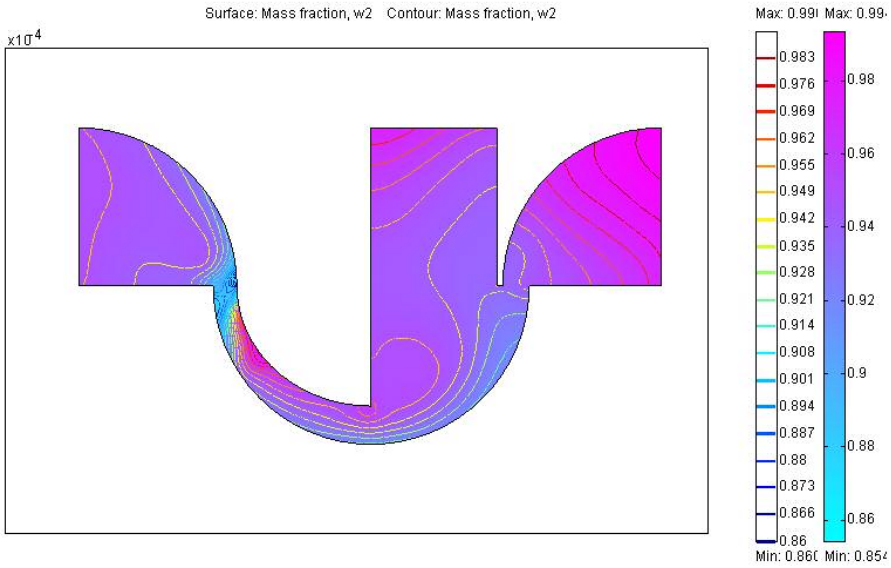

Figure 4.21: The Mode 1 N_2 Mass Fraction Distribution with N_2 Mass Fraction Gradients for a Pressure Ratio of 2.0

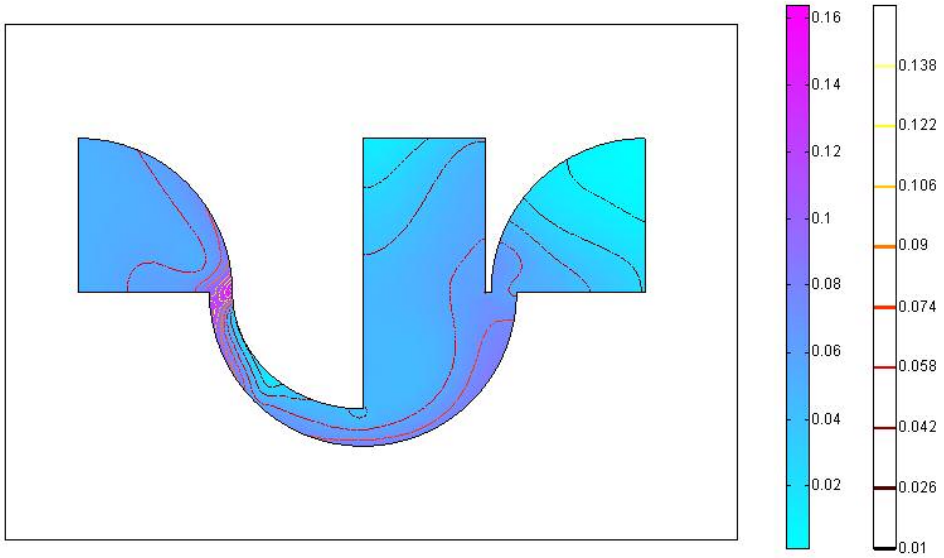

Figure 4.22: The SF_6 Mass Fraction Distribution with SF_6 Mass Fraction Contours for a Pressure Ratio of 2.5

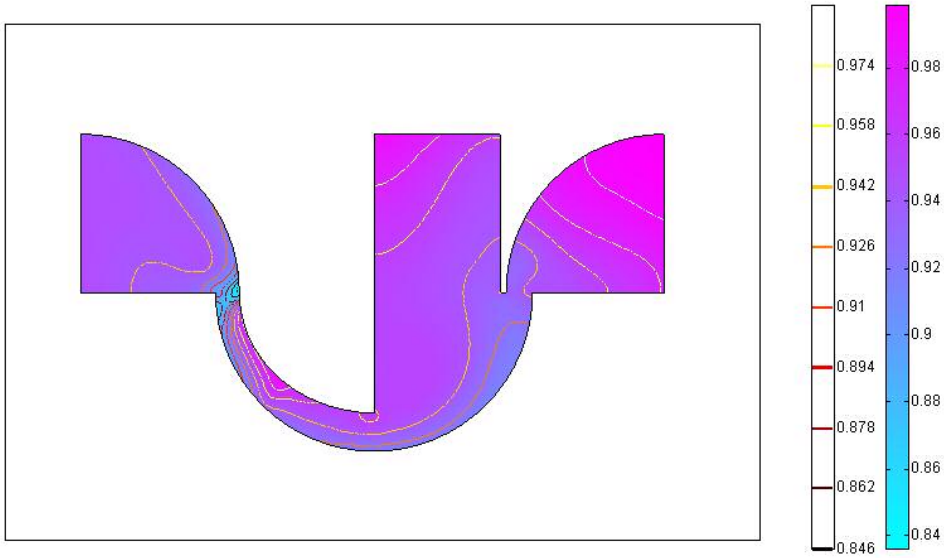

Figure 4.23: The Mode 1 N_2 Mass Fraction Distribution with N_2 Mass Fraction Contours for a Pressure Ratio of 2.5

4.6.4 Mass Flux Distributions (Mode 1)

The impact of changes in the boundary conditions is seen in the magnitude of the fluxes as shown in figures (4.11, 4.12, and 4.24-4.27). As the increase in pressure ratio creates a greater pressure gradient across the flow near the deflection wall, pressure diffusion increases thereby increasing the fluxes of N_2 and SF_6 normal to the streamlines. This, in turn increases separation.

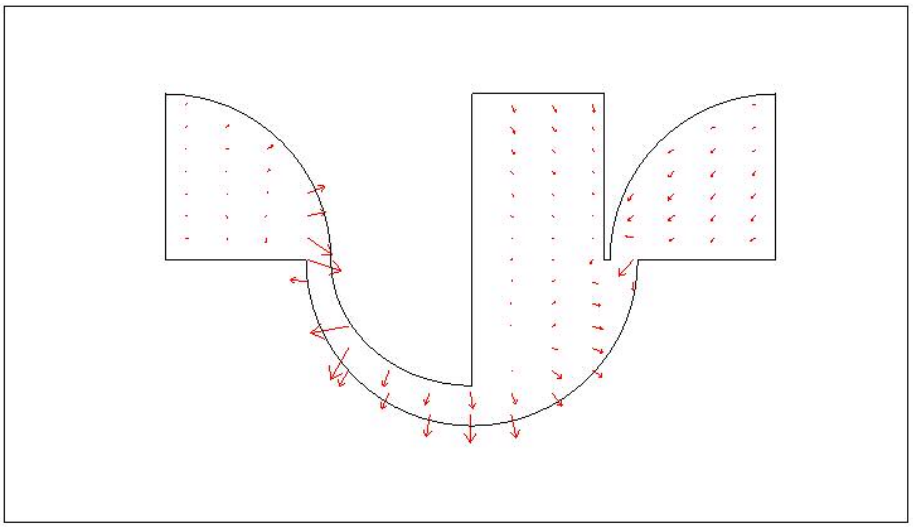

Figure 4.24: The Mode 1 SF_6 Mass Diffusive Flux Distribution for a Pressure Ratio of 2.0

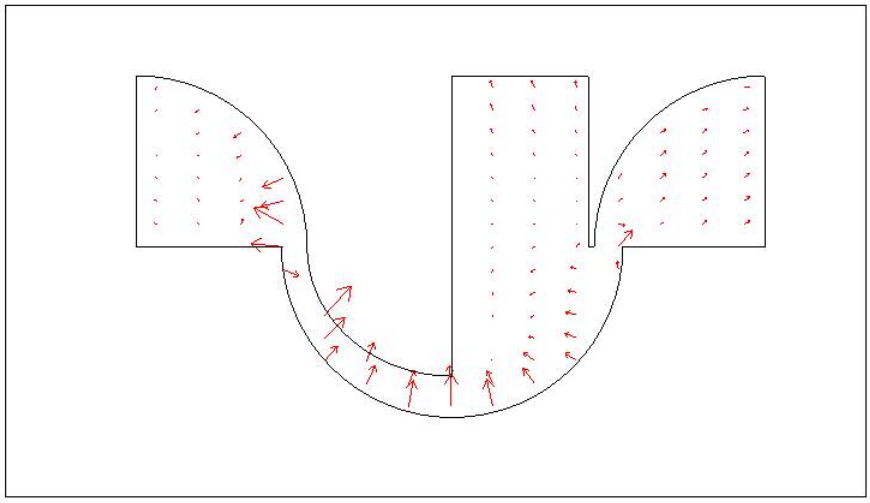

Figure 4.25: The Mode 1 N_2 Mass Diffusive Flux Distribution for a Pressure Ratio of 2.0

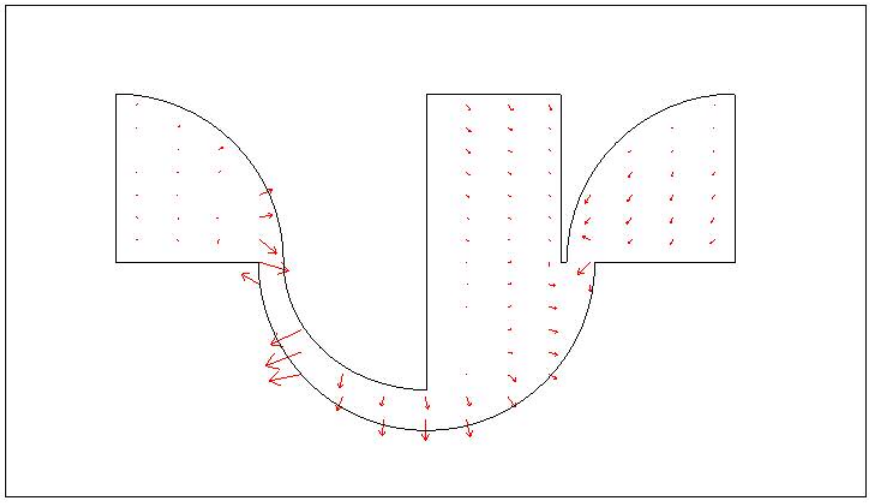

Figure 4.26: The Mode 1 SF_6 Mass Diffusive Flux Distribution for a Pressure Ratio of 2.5

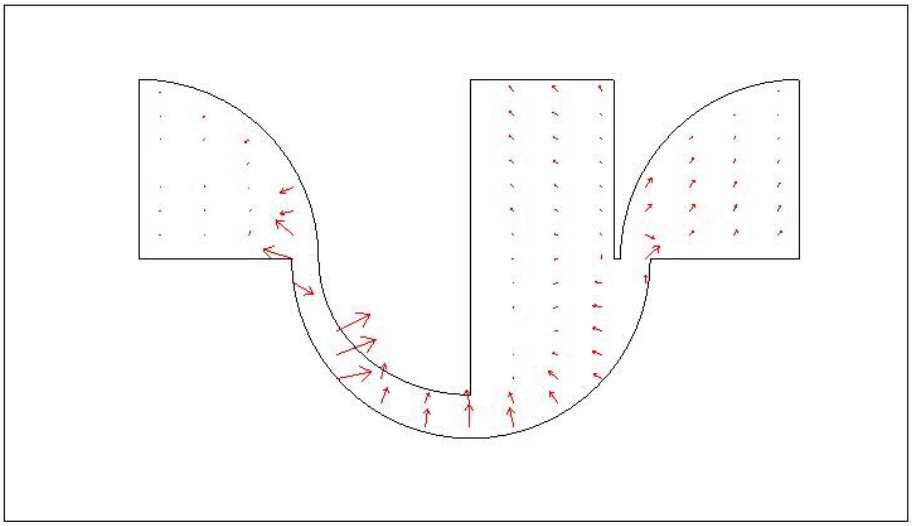

Figure 4.27: The Mode 1 N_2 Mass Diffusive Flux Distribution for a Pressure Ratio of 2.5

4.6.5 Pressure Distributions (Mode 2)

The impact of the inlet conditions on the pressure distribution generated through flow mode 2 is similar to the impact on flow mode 1. Figures 4.28-4.30 illustrate that the main impacts of increasing the pressure ratio are an increase in the magnitude of the pressure gradients near the deflection wall while the spreading out of the area of the SF_6 enriched region. As the pressure distribution is key in developing the mass fraction distributions, these changes in the pressure distributions due to the changes in the pressure ratio imply similar changes to the mass fraction and mass flux distributions.

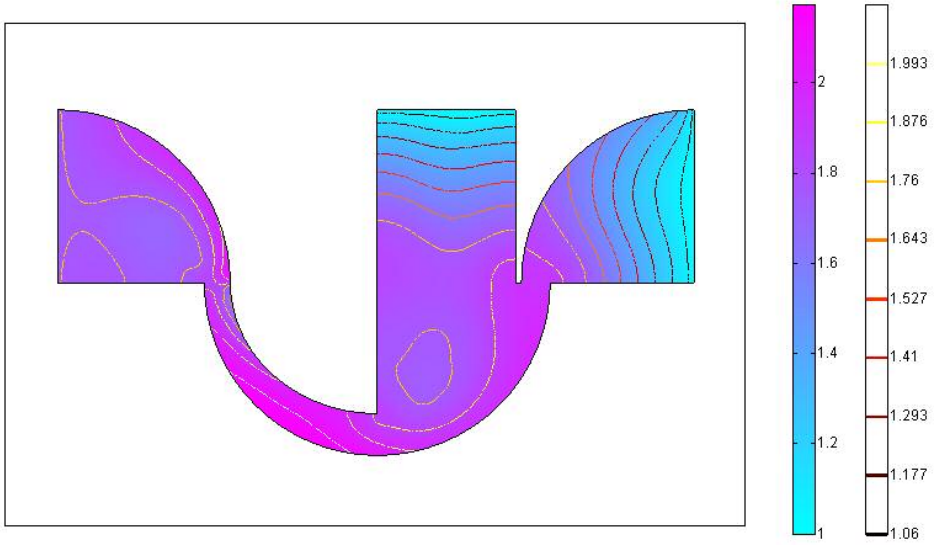

Figure 4.28: The Mode 2 Pressure Distribution for a Pressure Ratio of 1.75.

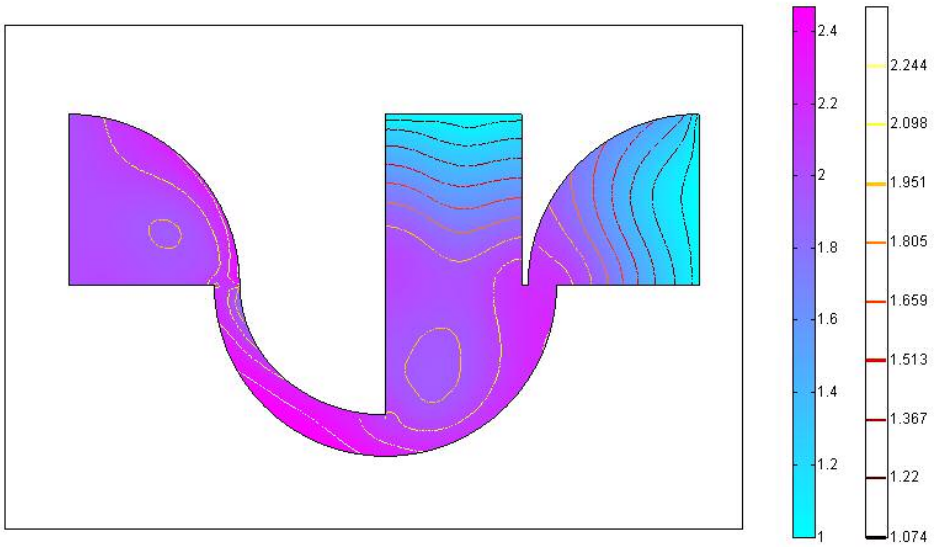

Figure 4.29: The Mode 2 Pressure Distribution for a Pressure Ratio of 2.0

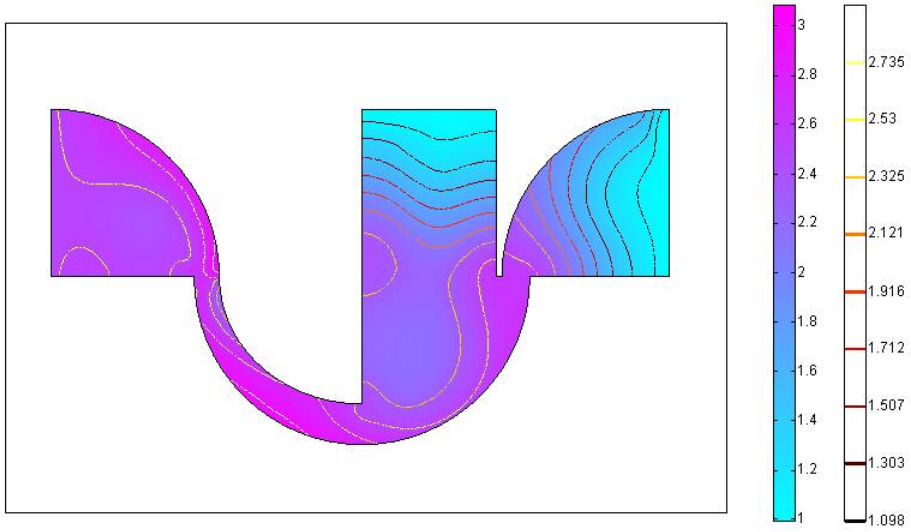

Figure 4.30: The Mode 2 Pressure Distribution for a Pressure Ratio of 2.5.

4.7 Residence Time

A key requirement of the device is the ability to provide a fast response time for detection. The time required for transit of a gas sample through the device is governed by the residence time. The residence time within the device was determined by measuring the average velocity and distance traveled along several streamlines, including those shown in figures 4.2, 4.16, and 4.17, and mass averaging the residence times along those streamlines. The number and location of the streamlines were chosen to cover a minimum of 95% of the mass flow rate. As the pressure ratio is increased, the mean flow velocity through the device also increases and therefore the residence time decreases, as shown in figure 4.31. The desired response time is on the scale of 0.1 milliseconds which is easily met by even the maximum device residence time of 12 microseconds.

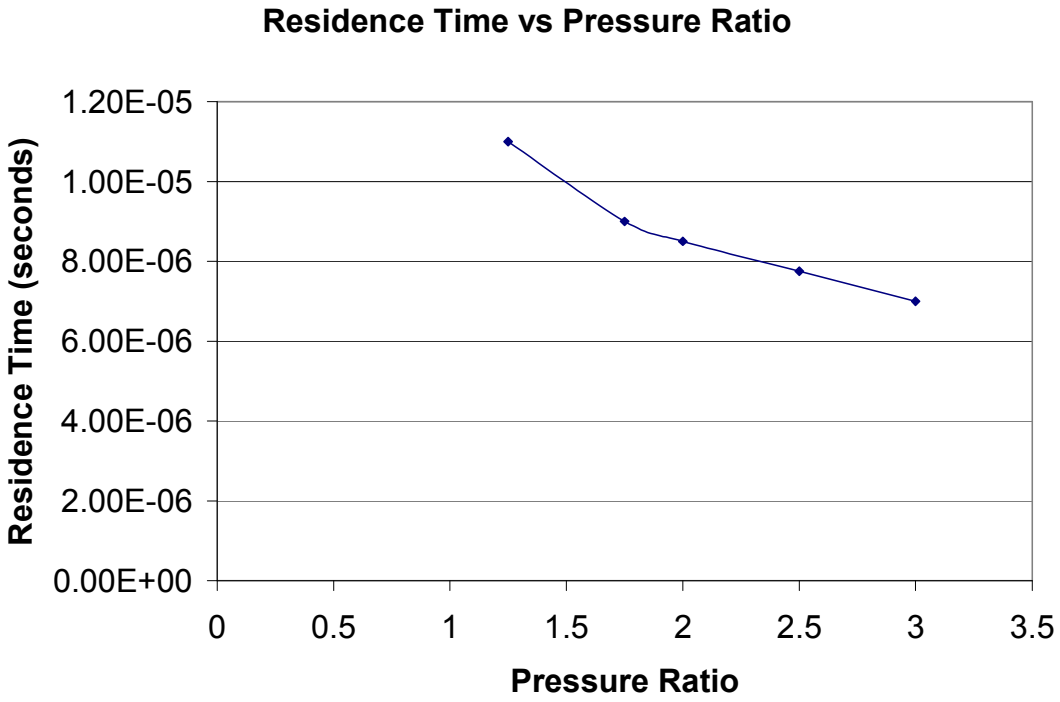

Figure 4.31: A Plot of Residence Time versus Pressure Ratio for Mode 1

4.8 Impact of a Change in Inlet Gas Mixture

The typical use of separation nozzles requires that they be cascaded to generate sufficient concentration of the denser species. The success of cascading requires that the separation factor remain significantly greater than 1 at higher SF_6 mass fractions. Therefore, a series of simulations was performed for a range of inlet mass fractions at a fixed pressure ratio of 2.5. Figure 4.32 shows that the separation factor increases with increasing SF_6 mass fraction until the mass fraction reaches a critical value. At this critical value, the ability of the device to further separate SF_6 is severely hampered.

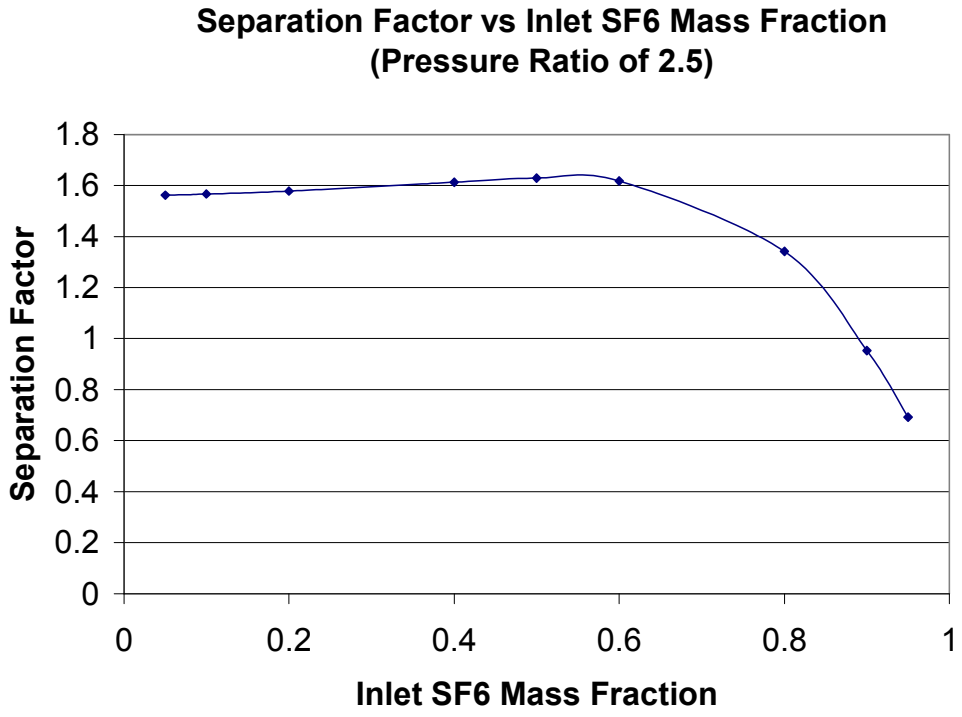

Figure 4.32: A Plot of Separation Factor versus Inlet SF_6 Mass Fraction

4.9 Comparison to Experimental Data

The results of the computational determinations of the separation factor for device 1 are presented in figure 4.33 along with data points showing the results of experimental measurements. The two curves correspond to the two different flow modes observed. The curves and data show that there is an optimum pressure ratio for maximizing separation although the peaks occur at different pressure ratios. The predictions for flow mode 1 fall within the error bounds of the experiment at low and high pressure ratios. Meanwhile, the peak in the experimental data seems to match the simulation results for flow mode 2 within the uncertainty limits of the experiments.

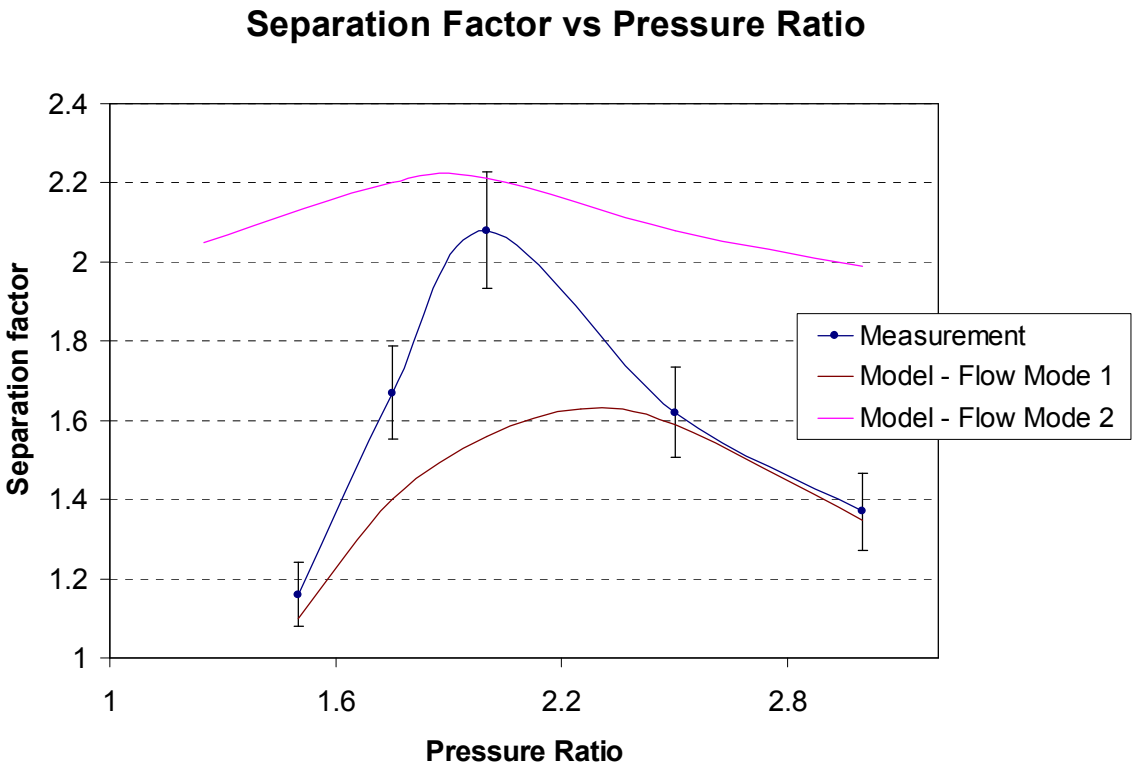

Figure 4.33: Plot of Separation Factor vs Pressure Ratio including Experimental Data for Device 1 with an Inlet SF_6 Mass Fraction of 5%

One possible explanation is that the flow is unsteady in the experiments and hops between modes at pressure ratios between 1.5 and 2.5. At the pressure ratio associated with peak separation factor in the experiments, the flow would spend more of its time in mode 2 and so would have a separation factor that is closer to the value associated with mode 2. In this scenario, the distance between the data point and the curve corresponding to each of the modes would provide a visual indication of the relative time spent in one mode versus the other. One way to check this hypothesis would be by acquiring more experimental data at pressure ratios below 1.5 and greater than 3 to see if they match the mode 1 solution. Another way would be to visualize the flow in the device using unsteady micro-particle image velocimetry.

Another possible explanation is that the second mode is not a physically realistic one and that the peak in the experimental data is caused by something else – possibly viscous effects – that is not accounted for in the numerical simulation. A key factor for consideration is the movement of the shock wave down the diverging nozzle section. According to the Navier-Stokes simulation without the diffusion equation, the shock wave reaches the exit of the diverging section at an approximate pressure ratio of 2.5. This phenomenon may be the cause of the spike in separation factor and the lack of the same significant movement in the solution based on the Euler equations indicates that the viscosity may impact the performance of the device in very significant ways.

Chapter 5: Conclusions and Future Work

Computational fluid dynamics has been used to investigate the flow field in an aerodynamic pre-concentrator being developed for environmental monitoring applications. The variation of separation performance with pressure ratio was found to be able to predict the overall trend of the experimental results with increasing pressure ratios. The simulation results fall within the uncertainty boundaries of the experiment at both the high and low pressure ratios. It was also found that the flow may be experiencing a shift in modes at the mid-range pressure ratios because the simulations of the second flow mode compare better to the experimental data at the intermediate pressure ratios. Therefore, the simulations appear to be a useful tool for understanding experimental measurements and for predicting the results of design modifications.

The results show that separation factors of 2 with an average residence time of approximately 10 microseconds are possible with this particular device. This level of performance is adequate for use as part of a cascaded multi-stage gas separation device. For example, a separation factor of 2 corresponds to the concentration of a 1 mole percent SF_6 mixture to a 1.6 mole percent SF_6 mixture. If this separation factor can be maintained in each of 10 cascaded nozzles, the output would be a stream of nearly 100 mole percent SF_6 achieved in only 0.1 milliseconds. However, it was shown that the separation efficiency of the device also falls dramatically at high SF_6

mass fractions. This means that it may be necessary to individually optimize the design at each stage in the cascade to maximize separation performance.

Since the separation factor is also expected to be a strong function of device geometry, it is possible that other configurations could provide better single-stage performance. For example, the simulations show that the primary factors influencing separation in the device are the inlet nozzle geometry, the skimmer location, and the radii of curvature of the various curved surfaces.

Therefore, it may be possible to improve the single-stage performance by increasing the radii of curvature of the device, modifying the converging inlet to shape the expansion to increase the diffusive flux through the nozzle throat, rounding the heavy fraction stream exit corner, and/or relocate the skimmer to match the location of the high pressure gradient area. It may also be beneficial to move the skimmer closer to the diverging nozzle exit to capture the higher pressure gradient before it begins to diffuse. Even a small increase in single stage performance could cut the number of stages required by a cascaded system in half.

The first step for future investigations is to determine how separation performance varies with device geometry. The pressure ratio for optimum separation performance will probably be different for different device geometries. Another investigation that should be completed is a study of the experimental apparatus to determine whether the first or second flow modes are realized within the separation device.

Appendix A

FEMLab provides three methods for specifying partial differential equations (PDEs) [43]. These methods are the coefficient, general, and weak forms. The coefficient form is unable to handle highly non-linear functions and therefore will not be discussed as the problem studied was highly non-linear.

General Form

The general form is given by writing the PDEs in the following form:

$$\begin{cases} \nabla \cdot \Gamma = \vec{F} & in \quad \Omega \\ -\vec{n} \cdot \Gamma = \vec{G} + \left(\dfrac{\partial \vec{R}}{\partial u} \right)^T \mu & in \quad \partial\Omega \\ 0 = \vec{R} & in \quad \partial\Omega \end{cases} \tag{A.1}$$

The first equation is the PDE, the second equation is the Neumann boundary condition, and the third equation is the Dirichlet boundary condition. The terms Γ, F, G, and R are coefficients that can be functions of the spatial coordinates, the solution $\vec{u}$, or spatial derivatives of the solution $\vec{u}$. The coefficients F, G, and R are scalar functions, Γ is the flux vector, and μ is the Lagrange multiplier.

Weak Form

The weak form begins with the general form, multiplies each term by an arbitrary test function, v, then applies Green's formula to complete an integration by

parts, and finally substitutes the Neumann boundary equation into the PDE. The resulting equations are:

$$\begin{aligned} 0 &= \int_{\Omega} \left(\nabla v \cdot \Gamma - vF\right) dA + \int_{\partial\Omega} v\left(G + \frac{\partial R}{\partial u}\mu\right) ds \\ 0 &= R \qquad\qquad on \quad \partial\Omega \end{aligned} \tag{A.2}$$

There are two key advantages to using the weak formulation. The first is the ability of the weak form to handle discontinuities. Since the test function, *v*, can be any function, it can be used to allow the weak formulation to have a solution whereas the strong form would have no meaning when these discontinuities exist. The second advantage is that the weak form guarantees that the solver will use the exact Jacobian. The weak form is able to ensure the use of the exact Jacobian because it utilizes all of the terms in equation (A.1) when solving for the Jacobian while the general solution only uses the coefficient terms when finding the Jacobian.

Variable Definitions

a	-	Nozzle Throat Width (m)
a_α	-	Activity of Species α (unitless)
A	-	Separation Factor (unitless)
c	-	Concentration (mol/m^3)
d	-	Nozzle Height (m)
D^T	-	Coefficient of Thermal Diffusion (m^2/s)
D_{ab}	-	Coefficient of Binary Diffusion (m^2/s)
E	-	Error Vector
err	-	Total Error
f'(U_0)	-	Jacobian Matrix
f(U)	-	Residual Vector
F	-	Body Force Vector (N)
g_A	-	Body Force Acceleration for Species A (m^2/s)
$\overline{G_\alpha}$	-	Partial Molar Gibbs Free Energy for Species α (J)
J_A^*	-	Molar Diffusive Flux of Species A (mol/m^2/s)
k_T	-	Thermal Conductivity (W/m/K)
Kn	-	Knudsen Number (unitless)
$\dot{m}$	-	Mass Flow Rate (kg/s)
n	-	Unit Normal Vector (unitless)
N	-	Degrees of Freedom (unitless)
p	-	Gas Pressure (Pa)
Q	-	Heat Generation (J)
R	-	Universal Gas Constant (J/mol/K)
S	-	Scaling Vector
T	-	Gas Temperature (K)
u	-	Gas Velocity Vector (m/s)
U	-	Solution Vector
w_1	-	Mass Fraction of Species 1 (unitless)
W	-	Weighting Vector
x_A	-	Mole Fraction of Species A (unitless)
δ	-	Differential Operator
δU	-	Newton Step
∇	-	Del Operator (unitless)
γ	-	Ratio of Specific Heats (unitless)
λ	-	Mean Free Path (m)
μ	-	Coefficient of Dynamic Viscosity (Poise)
ρ	-	Gas Density (kg/m^3)
φ_A	-	Volume Fraction of Species A (unitless)
θ_l, θ_h	-	Partial Cuts (unitless)
ω_A	-	Mass Fraction of Species A (unitless)

Bibliography

[1] C.-J. Lu, J. Whiting, R. D. Sacks, and E. T. Zellers, "Portable gas chromatography with tunable retention and sensor array detection for determination of complex vapor mixture," *Analytical Chemistry*, vol. 75, pp. 1400-1409, 2003

[2] S. D. Senturia, *Microsystem Design*. Kluwer Academic Publishers, Boston, 2001, pp. 2-3.

[3] C.-M. Ho, "Fluidics-the link between micro and nano sciences and technologies," *in Proc. MEMS 2001*, pp. 375-384, Interlaken, Switzerland, Jan. 21-25, 2001.

[4] A. Folch, A. Ayon, O. Hurtado, and M. A. Schmidt, "Molding of deep polydimethylsiloxane microstructures for microfluidics and biological applications," *Transactions of the ASME: Journal of Biomechanical Engineering*, vol. 121, pp. 28-34, 1999.

[5] A. Manz, N. Graber, and H. M. Widmer, "Miniaturized total chemical analysis systems: a novel concept for chemical sensing," *Sensors and Actuators B: Chemical*, vol. B1, pp. 244-248, 1990.

[6] D. J. Harrison, A. Manz, Z. Fan, H. Luedi, and H. N. Widmer, "Capillary electrophoresis and sample injection systems integrated on a planar glass chip," *Analytical Chemistry*, vol. 64, pp. 1926-1932, 1992.

[7] V. Srinivasan and J. W. Weidner, "An electrochemical route for making porous nickel oxide electrochemical capacitors," *Journal of the Electrochemical Society*, vol. 144, pp. 210-213, 1997.

[8] P. C. Simpson, A. T. Woolley, and R. A. Mathies, "Microfabrication technology for the production of capillary array electrophoresis chips," *Biomedical Microdevices*, vol. 1, pp. 7-25, 1998.

[9] J. P. Brody, Y. Han, R. H. Austin, and M. Bitensky, "Deformation and flow of red blood cells in a synthetic lattice: evidence for an active cytoskeleton," *Biophysical Journal*, vol. 68, pp. 2224-2232, 1995.

[10] C. B. Freidhoff, R. M. Young, S. Sriram, T. T. Braggins, T. W. O'Keefe, J. D. Adam, H. C. Nathanson, R. R. A. Syms, T. J. Tate, M. M. Ahmad, S. Taylor, and J. Tunstall, "Chemical sensing using nonoptical microelectromechanical systems," *Journal of Vacuum Science and Technology A*, vol. 17, pp. 2300-2307, 1999.

[11] S. Taylor, R. F. Tindall, and R. R. A. Syms, "Silicon based quadrupole mass spectrometry using microelectromechanical systems," *Journal of Vacuum Science and Technology B*, vol. 19, pp. 557-562, 2001.

[12] P. Siebert, G. Petzold, Á. Hellenbart, and J. Müller, "Surface microstructure/miniaturemass spectrometer: processing and applications," *Applied Physics A*, vol. 67, pp. 155-160, 1998.

[13] "http://www.chem.vt.edu/chemed/sep/gc." last uploaded 12/15/2005.

[14] E. T. Zellers, W. H. Steinecker, G. R. Lambertus, M. Agah, C.-J. Lu, H. K. L. Chan, J. A. Potkay, M. C. Oborny, J. M. Nichols, A. Astle, H. S. Kim, M. P. Rowe, J. Kim, L. W. d. Silva, J. Zheng, J. J. Whiting, R. D. Sacks, S. W. Pang, M. Kaviany, P. L. Bergstrom, A. J. Matzger, Ç. Kurdak, L. P. Bernal, K. Najafi, and K. D. Wise, "A versatile MEMS gas chromatograph for determinations of environmental vapor mixtures," *in Proc. Solid-State Sensors, Actuators and Microsystems Workshop*, pp. 61-66, Hilton Head Island, South Carolina, June 6-10, 2004, 2004.

[15] C.-Y. Peng and S. Batterman, "Performance evaluation of a sorbent tube sampling method using short path thermal desorption for volatile organic compounds," *Journal of Environmental Monitoring*, vol. 2, pp. 313-324, 2000.

[16] W.-C. Tian, S. W. Pang, C.-J. Lu, and E. T. Zellers, "Microfabricated preconcentrator-focuser for a microscale gas chromatograph," *Journal of Microelectromechanical Systems*, vol. 12, pp. 264-272, 2003.

[17] W.-C. Tian, H. K. L. Chan, S. W. Pang, C.-J. Lu, and E. T. Zellers, "Multiple-stage microfabricated preconcentrator-focuser for micro gas chromatography system," *Journal of Microelectromechanical Systems*, vol. 14, pp. 498-507, 2005.

[18] P. Lubicki, J. D. Cross, S. Jayaram, J. S. Zhao, and O. Ward, "Removal of nitrobenzene and volatile organic compounds using electron radiation," presented at 1997 IEEE Annual Report - Conference on Electrical Insulation and Dielectric Phenomena, Minneapolis, October 19-22, 1997.

[19] C. Schaper and A. Tay, "Electron beam patterning on permeable polymer membranes for nanolithography and microfluidic applications," presented at Proceedings of the Thirteenth Biennial University/Government/Industry Microelectronics Symposium, June 20-23, 1999.

[20] http://www.engapplets.vt.edu/fluids/CDnozzle/cdinfo.html last uploaded 12/15/2005.

[21] W. Ehrfeld, *Elements of Flow and Diffusion Processes in Separation Nozzles*. Berlin Heidelberg: Springer-Verlag, 1983.

[22] E. W. Becker, K. Bier, and W. Bier, "Trenndusenverfahren mit leichtem Zusatzgas," *Z. Naturforsh*, vol. A17, pp. 778-785, 1962.

[23] E. W. Becker, K. Bier, W. Bier, and R. Schutte, "Trenndusenentmischung der Uranisotope bei Verwendung leichter Zusatzgase," *Z. Naturforsch*, vol. A18, pp. 246-250, 1963.

[24] E. W. Becker, W. Ehrfeld, D. Münchmeyer, H. Betz, A. Heuberger, S. Pongratz, W. Glashauser, H. J. Michel, and R. v. Siemens, "Production of separation-nozzle systems for uranium enrichment by a combination of x-ray lithography and galvanoplastics," *Naturwissenschaften*, vol. 69, pp. 520-523, 1982.

[25] E. W. Becker, W. Bier, P. Bley, W. Ehrfeld, K. Schubert, and D. Seidel, "Development and technical implementation of the separation nozzle process for enrichment of uranium-235," *Am. Inst. Chem. Eng., Sym. Ser.*, vol. 78, 1982.

[26] E. W. Becker, "Development of the separation nozzle process for enrichment of uranium," *German Chemical Engineering*, vol. 9, pp. 204-208, 1986.

[27] S. Li, C. B. Freidhoff, R. M. Young, and R. Ghodssi, "Development of MEMS-based micronozzles for gas separation," presented at Materials Research Society (MRS) Spring Meeting, San Francisco, CA, 2004.

[28] P. H. Oosthuizen and W. E. Carscallen, *Compressible Fluid Flow*. New York: The McGraw-Hill, 1997.

[29] A. Beskok and G. E. Karniadakis, "Simulation of Slip-Flows in Complex Micro-Geometries," *Micromechanical Systems*, DSC-Vol. 40, pp. 355-370, 1992.

[30] S. Li, C. B. Freidhoff, R. M. Young, and R. Ghodssi, "Fabrication of micronozzles using low temperature wafer-level bonding with SU-8," *Journal of Micromechanics and Microengineering*, vol. 13, pp. 732-738, 2003.

[31] S. Li, J. J. Park, J. C. Day, G. W. Rubloff, C. P. Cadou, and R. Ghodssi, "Development of a fast-response microfluidic gas concentrating device," Paper no. WA11, Eurosensors XIX, Barcelona, Spain, 2005.

[32] S. Li, "Design, Fabrication, and Testing of Micronozzles for Gas Sensing Applications." Doctoral Thesis, Department of Electrical Engineering, University of Maryland.

[33] J. D. Anderson, *Modern Compressible Flow with Historical Perspective*. McGraw Hill, Boston, 1990.

[34] R. F. Probstein, *Physicochemical Hydrodynamics*. John Wiley & Sons, New York, 1994.

[35] R. B. Bird, W. E. Stewart, and E. N. Lightfoot, *Transport Phenomena*. John Wiley & Sons, New York, 2002.

[36] P. Deuflhard, "A modified Newton method for the solution of ill-conditioned systems of nonlinear equations with application to multiple shooting", Numer. Math., 22, pp. 289-315, 1974.

[37] A. Greenbaum, "Iterative Methods for Linear Systems," Frontiers in Applied Mathematics 17, SIAM, 1997.

[38] Y. Saad and M. H. Schultz, "GMRES: A generalized minimal residual algorithm for solving nonsymmetric linear systems," SIAM J. Sci. Statist. Comput., 7, pp. 856-869, 1986.

[39] J.R. Gilbert and S. Toledo, "An Assessment of Incomplete-LU Preconditioners for Nonsymmetric Linear Systems", Informatica, 24, pp. 409-425, 2000.

[40] Y. Saad, "ILUT: A dual threshold incomplete LU factorization," Report umsi-92-38, Computer Science Department, University of Minnesota, available from http://www-users.cs.umd.edu/~saad. Last uploaded 12/15/2005.

[41] http://mathworld.wolfram.com/L2-Norm.html last uploaded 12/15/2005.

[42] R. Verfurth, *A Review of a Posteriori Error Estimation and Adaptive Mesh-Refinement Techniques*, Teubner Verlag and J. Wiley, Stuttgart, 1996.

[43] FEMLab 3.1 Documentation, COMSAL AB